Training toward Advanced 3D Seismic Methods for CO2 Monitoring, Verification, and Accounting

Type of Report: Progress

Frequency of Report: Quarterly

Reporting Period: July 1, 2011 – Sept 31, 2010

DOE Award Number: DE-FE002186 (UH budget G091836)

Submitting Organizations: Department of Earth and Atmospheric Sciences
Allied Geophysical Lab
University of Houston
Houston, Texas 77004-5505

Preparers: Prof. Christopher Liner – P.I.
Phone: (713) 743-9119
Fax: (713) 748-7906
Prof. Bernhard Bodmann (UH Math)
Dr. Jianjun Zeng (research scientist)
Dr. Martin Cassidy (research scientist)
Qiong Wu (PhD candidate) … coordinator for this report
Jintan Li (PhD candidate)
Tim Brown (MS candidate)
Heather Yao (MS candidate)
Johnny Seales (BSc candidate)

Distribution List:

FITS	FITS@netl.doe.gov	DOE-NETL
Karen Cohen	Karen.Cohen@netl.doe.gov	DOE-NETL
Vanessa Stepney	Vstepney@central.uh.edu	UH Contracts Office
Jack Casey	jfcasey@uh.edu	UH EAS Department Chair
Laura Bell	lbell4@uh.edu	UH EAS Department Admin
Lee Bell	lee.bell@geokinetics.com	Geokinetics (Industrial partner)
Keith Matthews	kmatthews@fairfield.com	Fairfield (Industrial partner)
Subhashis Mallick	smallick@uwyo.edu	Univ. of Wyoming
Steve Stribling	SStribling@gmocks.com	Grand Mesa Production

CONTENTS

Executive Summary

This report presents major advances in progress made through the report period from June 1 to September 30 of 2011 for the CO_2 sequestration training project in the Dickman field, Ness County, Kansas (Figure 1).

We have identified and corrected a small depth conversion error due to local topography. This error was affecting accuracy of our gridded geological depth model, which in turn is the basis for our flow simulation grid.

Good progress has been made in our primary goal of simulating elastic wavefield data and populating a 3D multicomponent survey design. The workflow is almost finished and will allow scenario testing with shear waves and other wave types.

Frequency isolation filtering has identified features representing additional stratigraphic and structural details not readily visible in broadband seismic data. In particular, 41 Hz data indicates feeder channels related to a large meander channel seen in broadband data, and at 6 Hz there seem to be indications of large-scale fracture orientations. The channel feature has been confirmed by well log analysis, and the fracture trends are currently being validated.

Seismic modeling based on flow simulator output is progressing. There are substantial issues related to regridding from the blocky flow simulation grid to a fine-scale seismic parameter grid, but these have now been substantially solved. Initial acoustic finite difference modeling identifies CO2 effects, and elastic modeling is currently underway.

Geological modeling (June)

A major task planned for this Quarter was to include shallower layers, such as the Permian Stone Corral Formation and the Upper Pennsylvanian Heebner Shale Formation as possible seals, to the previous 3D geological model hanging on the Middle Pennsylvanian Fort Scott Limestone. During this task, one of the factors that affect the geometry of the subsurface stratigraphic framework was identified as a topographic effect. Possible correction schemes for this effect have been discussed.

Stratigraphic-controlled velocity model

In the construction of the deep layer geological model, a stratigraphic-controlled velocity model was built to convert the stratigraphic framework and the seismic attribute volumes, in order to tie features revealed by seismic attribute volumes to the corresponding stratigraphic window for the evaluation of their geological integrity. Without a vertical seismic profile, the stratigraphic control was enforced through two sets of geological input data for computing the velocity model: 1) surface or layer-averaged velocity computed from sonic logs at five well locations (two full penetrations) gridded to 100x100 ft cells, and 2) A correction data set by time-depth pairs on three major tops at each of the 17 well locations as reference points to correct the computed velocity model.

Comparing with the volume velocity model based on sonic log in the Elmore 3 well with limited penetration to the deep saline aquifer, the stratigraphic-controlled velocity model better described the lateral heterogeneity of the rock property due to the lateral interwoven lithology around the Mississippian Unconformity, and the vertical heterogeneity of rock property at reservoir scale. Depth-conversion using this velocity model resulted in a 3D stratigraphic grid of reasonable precision. Figure 2 shows the depth-converted Mississippian carbonate reservoir top (green surface with contours). The oil-water contact surface gridded directly from well top data, together with the locations of producers (solid dots), injectors (arrowed circles) and dry holes (crossed circles) were plotted to validate the precision of the model. The conversion reflects the subsurface geometry accurately with minor errors.

When building the velocity model for shallow layers, the topographic effect became evident as a distortion of the subsurface geometry while adding stratigraphic control. This case is common when integrating well data with a land survey with topography. Since seismic surveys for the Western Interior Planes (WIP) aquifers are all land surveys, to remove the topographic effect from the input stratigraphic control data for the velocity model computation is a common step in multi-scale data integration workflow.

Topographic effect

The well kelly bushing (KB) elevation is used as a proxy of the local topography in the Dickman area (Figure 3), containing five well locations with sonic logs that can be convert to velocity logs. Seismic data was acquired at land surface around the KB

elevation then corrected to the Seismic Reference Datum (SRD) at 2600 ft in this study. The contribution of topographic effects to the two-way time (TWT) was accounted for by topographic statics. Log measurements started from each well KB, which is 120-200 ft lower than the SRD. The elevation difference between five data wells ranges from 40 ft to 80 ft. Figure 4 is a sketch showing the difference between seismic data hanging on SRD and the well data hanging on local KB. At the two well locations, the vertical interval from SRD to the shallowest blue surface immediately beneath the KB contains two media (air and rock) of different thickness (SRD-KB and KB1-KB2, respectively). This difference was corrected in seismic data at the SRD. Without re-datuming the well data corresponding to the SRD to remove the topographic effect, the velocity model computed can cause recognizable distortion of subsurface geometry in depth-conversion, especially for shallower stratigraphic units.

This effect was recognized in the deep model shown in figure 2. The reservoir closure around wells with topographically-high KBs (red circle around Dickman 1 and 6 wells, red well heads) was pulled down slightly, meaning the structure around the Dickman 1 well is not high enough. The area around topographically-low KBs (blue circle, Sidebottom 6) is slightly tilted. Because the topographic difference is less than 2% of the depth of the stratigraphic window around the Mississippian Unconformity (figure 5, light blue horizon, around -4400 ft in measured depth (MD)), the distortion to the depth-converted model is small.

This effect is expected to be more significant for shallow layers such as the Stone Corral (1700 ft MD), and Heebner Shale (3700 ft MD). The topographic difference can be up to 5% of the total MD thickness of strata. As shown in figure 5, the KB surface is estimated to be within 200-300 ms level (dashed blue lines), while the two shallower formations are around -400 and -500 ms levels, compared with the stratigraphic window for the deep model between -830 to -880 ms level. The first attempt to build a stratigraphic-controlled velocity model including shallow layers has revealed large errors and failures in computation. Also, distortion of the deep section shown in Figure 2 became more visible, from a couple of ms error to up to 10 ms, more than 50% of the thickness of the stratigraphic target window.

Proposed scheme for topographic correction of geology data

The best way ofremoving the topographic effect is to re-datum the well data. For this purpose, the KB is considered as an artificial surface with time-depth pairs at five data wells. The TWT sampled from the KB surface at each data well location will be corrected by the difference $Z = SRD - KB$ using velocity of air. This surface with an estimated velocity map will serve as the shallowest surface for initial input to the velocity model computation. The surface data set will be re-adjusted by trail-and-error tests until the depth-converted model gains a reasonable precision at the five data wells. Then the correction of KB will be applied to all 17 wells.

With the new QC tools for the velocity model building process in Petrel 2010, the trail-and-error tests become straightforward and less time-consuming. The value for this work

is that the resulting correction scheme may be added to the workflow in multi-data integration for the modeling of WIP aquifer areas with land surveys and no VSP logs.

Elastic forward modeling and trace population (Qiong)

We gratefully acknowledge Prof. Subhashis Mallick of the University of Wyoming for access to his elastic reflectivity modeling code (anivec).

With anivec we can design a 2D geometry, assign forward modeling parameters, and calculate synthetic multicomponent shot records with radial, transverse, and vertical components. Each trace in the common shot gather is the simulated seismic response at a certain offset. Since the earth model is assumed to consist of horizontal layers, and each layer is anisotropic in our simulation, the resulting 2D shot record has radial symmetry in 3D. This means that given the 2D multi-component common shot gather, we can populate any trace in a 3D seismic survey design with the trace from the 2D synthetic gather with appropriate offset. Since each design trace has a different azimuth, the 2D synthetic trace must be rotated into acquisition components. The radial and transverse synthetic components are rotated using the azimuth angle into N-S (H1) and E-W (H2) survey design components. This projection process is referred as horizontal rotation.

Figure 6 is a parameter window snapshot of elastic forward modeling geometry and input parameters. The geometry is a 2D receiver line with one source located at the origin. Trace length is 2 s (2000 ms), time sample interval is 2 ms, beginning at zero offset 2000 receivers are simulated with a group interval of 10 ft resulting in a far offset of 20000 ft.

Figure 7 shows the input Vp and Vs for the forward modeling based on the Humphrey 4-18 sonic log. The shear wave log is computed assuming a constant Vp/Vs ratio of 2. The red line is the blocked log. And figure 8 shows the output result name assignments.

Figure 9 and 10 show the radial and vertical component of the 2D survey. Since the receivers are located along a radial line through the shot, and the shot has no transverse motion, the recorded transverse component of the 2D survey is zero. Since the simulation time was set to just 2 s, late arrival events have been wrapped to early times at far offsets. In future simulations, we will increase trace length to avoid this problem.

Geokinetics provided the Dickman II 3D survey geometry in SPS format, containing shot and receiver coordinates, elevations and cabling information (which receivers are live for which shots). The survey design contains 4233 shots, and 3547 receivers arranged in 28 E-W receiver lines. Since the survey area is small (about 9 square miles) we assume the data is cabled static, meaning all receivers are live for all shots.

Figure 11 shows relative position of one shot to all the receivers. Receiver line 1097, for example, has 197 receivers, each with a different azimuth, and y coordinates of all the receivers are smaller than that of the shot.

Populating the 2D synthetic traces to the 3D survey according to offset, and horizontally rotating the seismic response according to azimuth, we obtained a multi-component shot gather for the 3D survey. Notice that the 3D vertical component seismic response is obtained after populating process; horizontal rotation process is not applicable since the recording directions of vertical component in 2D and 3D are exactly the same. Transverse component of 3D survey is zero since the source has no transverse component.

Figure 13 (a) and (b) show the radial and vertical component of receiver line 1103.

CO2 Flow simulation to Seismic (Jintan)

The flow simulation output is composed of a series of properties which are fully dependent on the geology structure. Unconformities, truncation or pinch out, have been considered as missing sections. These points will be skipped when exported from the flow simulation model due to zero thickness, and have to be added back into the model with correct values for seismic simulation. The flow simulation grid is quite sparse and needs interpolation into a finer grid for seismic simulation. The following steps will be performed to prepare the flow simulation output for seismic simulation.

The 1st step is to write a program to find missing indices in the vector output and put the corresponding properties (simply assigned as zero) into the model. Then all these vectors can be sorted into a 3D model with NX, NY, NZ points in each direction. The 2^{nd} step is to again assign correct depth values affected by the truncation or pinch out, but this will not affect other properties and they still remain as zero. Based on the zero thickness criteria, if the depth is zero at some point it means the depth is unchanged from layer above. Figure 14 shows what the real geology structure looks like in a 2D example, and Mississippian porous carbonate is our CO2 sequestration target. Table 1 shows the relationship the simulation layers of different geology formations.

The next step is to assign the correct index for all the fluid properties at the correct depth. The input simulation model has dimensions (33,31,32) in (x, y, z) direction. This is challenging because the simulation layers vary with depth except for the top four layers. Since they are not evenly spaced, I generate a new zero matrix with equal depth spacing (dz=10ft), and thus there are more points in Z direction. The procedure is to read in the depth first, and find its correct index and assign all the corresponding properties at that index. For CO_2 saturation this completes the process, but other properties (Z,P,T) are interpolated from nearby layers as needed.

The velocity model calculation uses Gassmann's fluid substitution for the first and last year of CO2 injection monitoring. The velocity model is interpolated into a finer grid (dx=5 ft, dz=5 ft) in Seismic UNIX (SU) shown in Figure 15. The major difference lies in the Mississippian porous carbonate, mainly due to the CO_2 injection. The acoustic finite difference modeling employed a 35 Hz point source (Figure 16) at the surface as well as a plane wave source parallel to the surface (Figure 17). They both show seismic changes before and after CO_2 injection, edge effects and numerical dispersion will be corrected in future simulations.

Ultra-Narrow band filtering (Johnny)

Structural characterization through narrow-band decomposition has been investigated. The initial plan was to build a trapezoidal frequency filter with a 2 Hz span across the top in order to isolate specified frequencies. The filter designed in SeismicUnix (SU) has proved to be quite beneficial for producing isolated frequency volumes for interpretation to test our hypotheses.

The filter was originally built in SU and Kingdom SMT, with the SU filter appearing to have better frequency isolation. Figure 18 shows the results of the broadband, 6 Hz, and 41 Hz filters as plotted in SU to a common scale. These two frequencies were chosen based on intriguing features observed in 848 ms time slice scans for various frequency filters separated by 1 Hz. At 6 Hz, there are linear features seen that need further investigation, and at 41 Hz, there appears to be additional channel detail than seen on the broadband data.

In Figure 19, the broadband data is depicted in the 848 ms time slice. The main channel feature is easily seen in the eastern side of the image and meandering south to north. There are no definite linear features depicted within the figure, nor any indication of a tributary type channel feed in to the main channel feature. Figure 20 shows the 848 ms time slice at 6 Hz. There are multiple sets of features within this data that suggest possible fracture orientations (yellow lines).

Linear features in seismic time slice data automatically draw suspicion of being acquisition footprint, meaning amplitude stripes parallel to shot or receiver line orientation. The Dickman 3D shooting geometry is shown in Figure 21. The source lines are aligned N-S, and the receiver lines E-W. Comparing this to the 6 Hz data, we find the 6 Hz linear features do not align with acquisition geometry and are therefore more likely geological in nature.

Figures 22, 23, and 24 show the sequence of 40 Hz, 41 Hz, and 42 Hz time slices at 848 ms. The purpose of viewing these is to show persistence of a possible channel feature in the decomposed data. This channel feature is not seen in the broadband data of Figure 19, and is highlighted in the decomposed data by the yellow arrow highlighting the secondary, or feeder, channel location. We hypothesize this feature is a tributary feeding into the main channel. Figure 25 shows a modern analog in coastal Georgia. The area highlighted with the yellow circle shows a smaller tributary channel feeding in to a main channel with the channel bar being visible as is the case in our data.

To confirm the existence of the channel feature seen in the decomposed data, log information for four wells lying in the main and tributary channel features were investigated. A cross section through these wells (Figure 26) was extracted from the 41 Hz data. Wells 1 and 2 lie either in or in close proximity to the tributary channel feature, and wells 3 and 4 lie within the main channel feature. The suspected channel feature is highlighted in this figure by the same yellow arrow as depicted in earlier figures showing the relation of this channel and the composed cross section.

A cross section through the wells is hung structurally and based on the interpretation of the gamma ray (GR) and resistivity (RES) logs for these four wells (Figure 27). The logs are shown equally spaced. Basic lithology can be determined from the GR log. From lowest to highest GR values, we have limestone (LS), sandstone (SS), and shale (SH) rock types. This is very important to our interpretation because the sequences in which these rock types occur can be correlated to the depositional environment. The black arrows placed on the GR logs in Figure 28 for each well indicate fining upwards sequences. These sequences are defined as moving from an area of lower gamma, or sandstone, to an area of higher values of gamma, or a muddier rock. This sequence is then capped at the top by a flooding event indicated by a sharp drop from high to lower gamma. With upward fining sequences identified for each well, an interpretation of the lithology and environment may be made.

The interpretation shown in Figure 29 supports the hypothesis of hidden channel features being decipherable through narrow-band decomposition. The base of the interpretation focuses on the blue area of the cross section representing Mississippian LS and dolomite. Above this, there are fining upwards sequences represented from base to flooding surface by yellow (SS) to gray (SH). Although hard contacts appear to be present within this interpretation, with respect to the fining upwards sequences, it should be noted that all contacts are assumed to be gradational with the exception of the flooding surfaces between the SH and overlying SS. Comparing features of sequences exhibited by the known channel feature and the suspected channel feature, it can be seen they are very similar. According to classification systems, these fining upwards sequences are characteristic of channel systems and therefore, it can be concluded that these well logs were taken from channel environments. We conclude the 41 Hz data are, indeed, indicating tributary type channel features feeding into the main channel system seen in the broadband data.

Simple frequency filters can provide valuable data decomposition to the interpreter. This data can identify possibly fractured areas that need further investigation, and secondary channels features that may be unidentifiable in full bandwidth data. This capability can aid reservoir characterization, including our CO2 sequestration efforts.

Fracture characterization (Tim)

Narrow band frequency isolation (NBFI) at 6 Hz in the Dickman 3D seismic data reveal anomalous NW-NE striking features at 848 ms, an approximation to the Mississippian-Pennsylvanian unconformity (figure 30). In order to validate these features, our investigation proceeds along three paths: 1) post stack attribute analysis, 2) prestack analysis, and 3) well log analysis. The two former relate to large scale fracturing or faulting trends while the latter (the focus of this report) relates to small scale jointing and fracturing indicators. We can assume however, that log-scale indicators test our hypothesis that the low frequency anomalies are in fact related to fracture networks. A summary of the analyses is provided:

1. Post stack attribute analysis: The constrained least-square spectral analysis (CLSSA) algorithm will be applied to our seismic volume (courtesy of Prof. John Castagna). This algorithm gives excellent time frequency resolution, compared to other spectral decomposition methods, enabling spectral inversion (thin bed determination) and improved fault/fracture characterization (Puryear and Castagna, 2008).

2. Pre stack analysis: If paleo-stress effects persist in the local stratigraphy, then evidence will be prevalent in the pre stack data. Specifically, azimuthal anisotropy (the dependence of velocity on azimuth) will exist due to sub-vertical fracture geometry. The primary methods that express these anisotropic effects include amplitude variation with offset and angle (AVAZ) and velocity variation with azimuth (VVAZ). The former provides better resolution because it only considers the reflection boundary. The latter considers anisotropic effects over a larger interval and therefore provides lower resolution. Both methods are being considered and information concerning the theory and practical applications can be found in various works by Leon Thomsen and Ilya Tsvankin.

3. Well log analysis (The focus of this report): The optimal data required for this investigation would consist of borehole image logs as well as detailed core descriptions, both would provide a direct method for identifying fractures. These types of data quantify fracture geometry and density as well as indicate whether the fracture is open or healed (Martinez et al., 2001). Unfortunately, image logs were not acquired at Dickman and core information is rather scarce, therefore an indirect approach will be implemented in which conventional well logs will be analyzed.

Well log analysis

Conventional well logs refer to those that are routinely collected by industry and often respond indirectly to the presence of fractures. Excluding a change in lithology, a particular log's signature may express an abrupt deviation, often in the form of a spike, when encountering a fractured interval. Although not a robust method, these anomalous occurrences can make fracture identification a more objective process. Figure 31 provides a list of conventional logs used for fracture characterization and also describes the particular log's response to fractured rock. For a more comprehensive explanation on log

responses to fractures refer to "Crain's Petrophysical Handbook" (http://www.spec2000.net/01-index.htm). Indirectly quantifying the fracture density of a particular interval requires the implementation of a fuzzy inference system (FIS) similar to the work done by Martinez et al. (2001).

A fuzzy inference system is a process that maps an input value to an output value using a set of membership functions and rules that are based on human expertise of the problem. For our purposes, we are creating a non-linear translation from log values (the input) to fracture index (the output). The fracture index (FI) is not an inherent property of a particular interval of rock, but rather a relative scale of fracture intensity. For a more detailed account of FIS theory refer to Roger et al. (1997).

An example of a FIS schematic is shown and explained in Figure 32. The workflow for fracture characterization is as followed:

1. Application of a 6-point running average filter was applied to designate a background to be compared with the actual log value.
2. A linear scaling function was used to normalize the different log scales using the following equation:

   $$Z_i = \frac{X_i - a}{b - a}$$

   Where Z_i is the scaled vale, X_i is the log value, while a and b are the minimum and maximum log values respectfully. The scaled log values will range between 0 and 1.
3. Sigmoidal membership functions created for inputs and outputs (figure 33).
4. Linguistic operators define rules for identifying zones with high fracture probability
5. Defuzzification process.
6. Plot and analyze results.

It is important to note that only 2 wells in the Dickman survey, Humphrey 4-18 and Sidebottom 6, have the sufficient log information for this process. The proximity of the wells to the seismic coverage and to the spectral anomalies (Figure 30) is not optimal. However, the goal is to understand whether the particular interval of rock near the Mississippian-Pennsylvanian unconformity is in fact significantly fractured enough to yield anomalies in the post stack seismic volume. Therefore, if results indicate that this same interval of rock in the two wells have high and comparable fracture indexes, a strong case can be made that the low frequency anomalies are in response to sub-resolution fracture networks.

An experimental FIS was implemented for a set of logs (Figure 34) belonging to Sidebottom 6. The zone of interest is a Mississippian carbonate section just below the unconformity. Parameters and results are displayed in figure 35. Results do show specific zones having high fracture indexes (zones of high fracture probability). However, in order to validate these results drilling reports and core data will have to be obtained and compared, which consequently would be the next step in this investigation. Implementation of fuzzy interference systems will continue as more direct fracture

indication data becomes available. Some core and other logging information can be accessed through the Kansas Geological Survey (KGS).

Fuzzy inference systems provide a mean of indirectly quantifying fracture intensity from well logs. Rectification of FIS results requires direct information such as core descriptions and drilling reports. Due to the scarcity of this data, although some is available, pre and post stack analysis will be the primary focus of future work.

First break picking algorithm (Heather)

During a joint CO_2/AGL/Geokinetics meeting, Dr. Bernhard Bodmann suggested that one could determine first arrivals in seismic traces based on computing standard deviation of noise levels in the data. The proposed method uses the standard deviation of the noise (before signal arrival) in order to quantify the amount of amplitude standout that will be considered a signal arrival, and deduces P-wave first arrival times. Moreover, because of its statistical nature, the estimation of arrival times comes with a probability of a false positive/arrival, which can be adjusted by the user to trade off sensitivity against specificity.

Method:

1. User chooses the noise window and the signal window (Figure 36). These windows are assumed to contain, with certainty, only noise, or noise with a possible superposed signal arrival, respectively.
2. User chooses the threshold level β, a quintile for the noise distribution, which controls the probability of the algorithm generating false positives in the presence of pure noise.
3. Compute noise mean.
4. Compute noise Standard Deviation.
5. Divide entire trace amplitude by noise standard deviation, call this X.
6. Correct for the calculated mean.
7. Assign a new value Y using the following criteria.
    a. If $|X| \leq \beta$, then Y = 0
    b. If $\beta < |X|$, then Y = 1
8. Find first m consecutive occurrences where $Y \neq 0$, and this is our first p-wave arrival.
9. Correlate this specific Y to its sample number and we have the arrival time.

Constraints:

1. The definition of the noise window and signal window is based on the assumption that in the noise window, there's not any signal, but in the signal window, it's allowed to have some noise.
2. The consecutive number m is an integer, but the threshold β, also called beta, standard deviation threshold level, can be any positive float number.

Based on the method described above, a 'suaglpickr' is developed as a Seismic Unix (SU) command using C program. This code is designed to pick the first arrival time for multiple traces and calculate the mean time and standard deviation for the time.
In the code, several default parameters are defined as:

```
tn1=0       begin time(s)of the noise window
tn2=0.15    end time (s of the noise window
ts1=0.15    begin time (s) of the signal window
ts2=0.3     end time (s) of the signal window
m=2         consecutive samples over threshold
            to be considered as signal
beta=2.2    standard deviation threshold level
filename=output.txt           output txt file
out=1       output is origAmp/noiseStdDev with
            zero before 1st break pick
            =2 output zero trace except 1st break
            pick has unit amplitude
```

We assume that z represents the standard deviation normal variable. P is the probability.
If: $P(|z| \geq \beta) = P$
Then: $P(|z_1| \geq \beta, |z_2| \geq \beta, \ldots |z_m| \geq \beta) = P^m$
Therefore: α=(signal window length – $m + 1$) P^m

The user needs to input the data traces and filename to store the result.
The algorithm also includes a probability calculation to show the false positive within the signal window in the trace for the given threshold level and the number of consecutive values above the threshold. Users can adjust the m, β, or length of noise window or signal window to get a feasible false positive probability for the trace.

The output SU data is input amplitude divided by noise standard deviation and the result is put into the text file, showing noise window, signal window length in seconds, signal window length in sample number, β, m, probability of error, first arrival time sample number, first arrival time in second, and probability of false positive anywhere per trace. Also, trace number, pick time per trace, mean of the first pick time in second, variance, and standard deviation for the first pick in second are calculated in the report as well.

Here's an example using this algorithm to pick the first breaks. In this example, there are 2 traces as input data, each trace has two spikes with consecutive sample numbers of 50, 51, and 55, 56. The command 'suaglpickr' is applied on the input data, with parameters tn1=0.0 tn2=0.17, means the noise window is redefined from 0 to 0.17 second, and ts1=0.17 ts2=0.3 means the signal window is redefined from 0.17 to 0.3 second. A=2.25 represents the threshold level and m=2 shows we consider it as first arrive pick until there are at least 2 consecutive spikes occurring.

The output is shown in Figure 38.

The output trace data gives the first arrival sample number as 49 and 54, which match with the input, therefore, this algorithm is proved to be correct.

The output text files are shown in Figures 39 and 40. The output data for trace 1 and trace 2 give the first arrival pick in sample number and time, and validate the results. The probability of false positive anywhere is 0.020125, which is a relatively low number, which means the parameters for the threshold β and m are chosen reasonably.

Figure6 below shows the summary of the traces and calculate the mean value in second for the pick time and standard deviation for the pick.

Permian Basin residual oil zones (Martin)

The University of Houston is joining the University of Texas Permian basin (UTPB) in a project funded by Research Partnership to Secure Energy for America (RPSEA). The project is for Identifying and Developing Technology for Enabling Small Producers to Pursue the Residual Oil Zone (ROZ) Fairways of the Permian Basin San Andres formation.

In the Permian Basin of Texas thick residual oil zones (ROZs) are present immediately below shallow oil fields long productive from the San Andres dolomite. These ROZs, some over 200 feet thick, contain 20 to 40% oil in pore spaces but the oil cannot be produced by conventional production techniques, including water flooding. The amounts of oil in the ROZs can be up to one billion barrels in place in individual accumulations. In favorable circumstances it is estimated that 10% to 15% of that oil can be recovered by CO2 flooding. Full scale production is underway in the ROZ of Seminole field of the Permian Basin and that project may recover as much as 150 million barrels of new oil in the next 20 years from below the pay in the field above. (Hess, 2010 presentation).

ROZs are present under both large and small fields in the Permian Basin and perhaps exist as pods of partially oil saturated San Andres dolomite where there are no other fields.

The University of Houston's part of the large complex three year study is to examine the organic geochemistry of oil and water from ROZs, and the geochemistry of oil extracted from rock and water samples in and around ROZs to determine markers that may confirm the presence of unrecognized ROZs worthy of production.

Already two samples of oil and one of water from a producing ROZ have been acquired and preliminary analyses of oil and water have been made under a separate related contract with the UTPB (DOE Next Generation EOR Project). Differences have been detected between producing zone oil and ROZ oil in a Permian Basin San Andres dolomite reservoir and hydrocarbons have been extracted from black sulfur water.

Analysis of samples in the RPSEA ll project awaits completion of final paperwork from the granting agency and UTPB.

Work plan for the next quarter

Advancing to the 2D elastic wave forward modeling for the current velocity models, as well as the inverted Vp, Vs and density models from the prestack seismic data and compare the results.

Cost and milestone status

Baseline Costs Compared to Actual Incurred Costs

7/1/11 – 9/30/11	Plan	Costs	Difference
Federal	$36,668	$49,559	($12,892)
Non-Federal	$4,063	$0	$4,063
Total	$40,730	$45,559	($8,829)

Forecasted cash needs Vs. actual incurred costs

Notes:
(1) Federal plan amount based on award of $293,342 averaged over 8 reporting quarters.
(2) Non-Federal plan amount based on cost share of $32,500 averaged as above.
(3) Cost this period reflects salary for J. Zeng (3 mo), Q. Wu (3 mo), J. Seales (3 mo), and C. Liner (1 mo).

Actual progress compared to milestones

Continuing personnel

Prof. Christopher Liner is Principle Investigator and lead geophysicist. He is a member of the SEG CO_2 Committee, Associate Chairman of the Department of Earth and Atmospheric Sciences, Associate Director of the Allied Geophysical Lab, and has been selected to deliver the 2012 SEG Distinguished Instructor Short Course.

Prof. Bernhard Bodmann is co-PI for the Geokinetics project and a member of the University of Houston Mathematics Department.

Dr. Jianjun (June) Zeng has been working exclusively on this project since Dec 2007 and is lead geologist.

Dr. Martin Cassidy is a research scientist in the Department of Earth and Atmospheric Sciences at the University of Houston.

Ms. Qiong Wu is a graduate PHD student in geophysics who joined the project in January 2010 as a research assistant. She will be funded year-round out of the project.

Mr. Johnny Seales is an undergraduate student majoring in Geology and Geophysics. He is also a U.S. Army veteran, having served in Iraq. He will be funded year-round from the project. He anticipates earning his undergraduate degree in Dec. 2011.

Ms. Jintan Li is a 2nd year PhD student in geophysics who joined the project in Aug 2009. She is funded by Allied Geophysical lab at this time. Her thesis will be time-lapse seismic modeling (4D) for conducting dynamic reservoir characterization of the Dickman Field.

Ms. Heather Yao is a 1st year MS student in geophysics.

Technology transfer activities

Five SEG expended abstracts were submitted to 2011 SEG Annual Meeting. They are:

Mapping Deep Structure in Ness County, Kansas from 3D Seismic and Minimal Well Control
Shannon LeBlanc*, Christopher Liner, and Jianjun Zeng

Comparison on shear wave velocity estimation in Dickman field, Ness County, Kansas
Qiong Wu*, and Christopher Liner

References

Appendix A: AAPG abstract

AAPG 2012, April 22-25, 2012, Long Beach, CA, Theme 10, Chair: Steven Getz,
"Geology/Geophysics Integration Case Studies session", dead line Sept. 22, 2011

Study of faults and fractures in Mississippian carbonate reservoirs by multi-scale data integration: a geological modeling case in the Dickman Field of Ness County, Kansas State

Jianjun Zeng[1], Christopher L. Liner[1], and Johnny Seales[1]
Earth & Atmospheric Sciences, University of Houston, Houston, TX
(jzeng@mail.uh.edu)

Fault and fracture analysis is an important step to guide the 3D reservoir property gridding for the Dickman Filed as a potential CO2 sequestration site. Due to the lack of standard logs and borehole images for such analysis, discontinuity patterns visualized by multiple seismic attributes were displayed in their original geological occurrence and tied to stratigraphic units at the reservoir scale to evaluate their geological integrity. The evaluation was based on the understanding of regional deformation history; the distribution patterns of fault/fracture zones predicted by a carbonate deformation model; the structural-controlled maturity of karst topography; and the fault and fracture indicators from sparse well logs, core descriptions and measurements.

The motion of major faults visualized by the SPICE attribute volume reflects the influence of the latest structural episode. Well tops, thickness and lithology data were used together with seismic images to determine the relative motion of blocks across faults during earlier structure episodes. Indirect indicators of differential up-lifting across faults, such as the relative roughness of karst-topography extracted from attributes, were also used to restore the multi-episode deformation associated with faults. Possible fractured zones extracted from six geometry attributes revealed different vertical and lateral patterns of discontinuity. These patterns were classified into two geometric categories: the unconfined features penetrating multiple litho-zones; and confined features mostly within an individual litho-zone. The former, best viewed by plane-extraction from ANT volumes, are mostly structural and associated with major faults. The latter are mostly none-structural and best viewed as varying density patterns while marching depth slices of Chaos and Variance volumes. These patterns can be more indicative of post-depositional changes, and some could be related to the “intra-strata” features observed in the Middle Mississippian cores in nearby Schaben Field.

Multi-scale data integration improved the confidence of fault and fracture interpretation based on seismic attributes. Such interpretations helped in the reconstruction of multi-episode deformation history of the area. Several major NW-trending faults and associated fractured zones are likely fluid conduits, and a NE-trending fault served as the sealing fault for the hydrocarbon-producing structure.

Tables

Sim Layer No.	VerticalPerm	Porosity(%)	Formation Name
1-6	10 md	18.2	Shallow Reservoir layers
7-8	0.01 md	20.0	Two Seal Layers
9-10	0.7 Horizontal Perm	10.3	Ford Scott Limestone
11-13	0.5 Horizontal Perm	19.1	Cherokee
14-15	0.5 Horizontal Perm	16.5	Lower Cherokee
16	0.7 Horizontal Perm	14.8	Mississippian Unconformity
17-20	0.7 Horizontal Perm	20.0	Mississippian Porous Carbonate
25-32	0.7 Horizontal Perm	22.45	Mississippian Osage and Gillmor City

Table 1. The relationship between the simulation layers and geological layers.

Figures

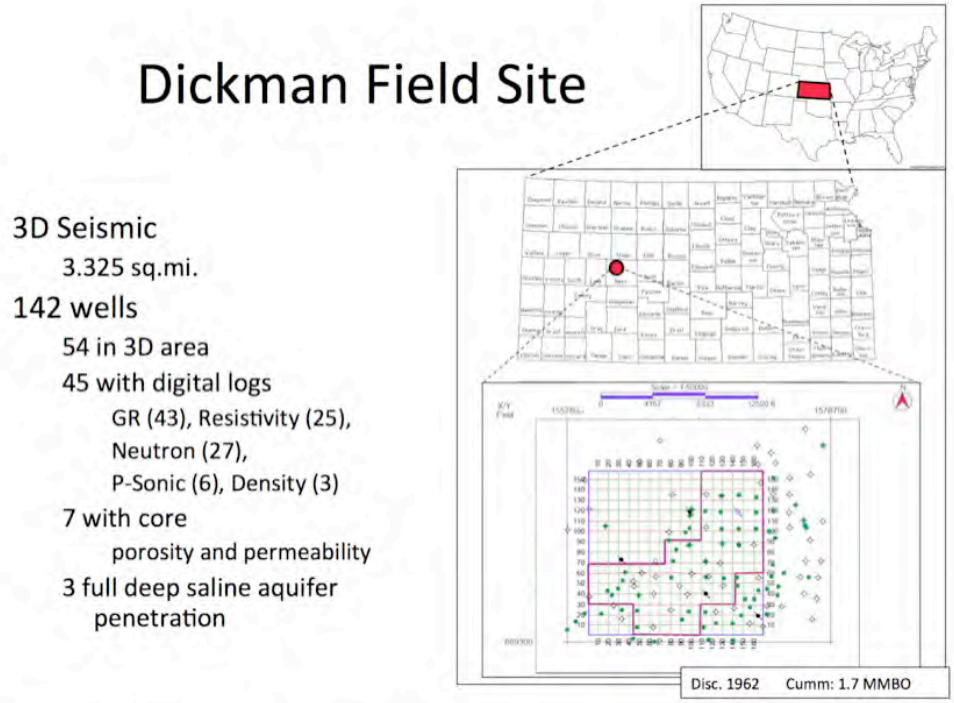

Figure 1. Area map depicting the location of the project area, Dickman field, Ness County, Kansas. On detail map, live 3D seismic area is shown as purple polygon.

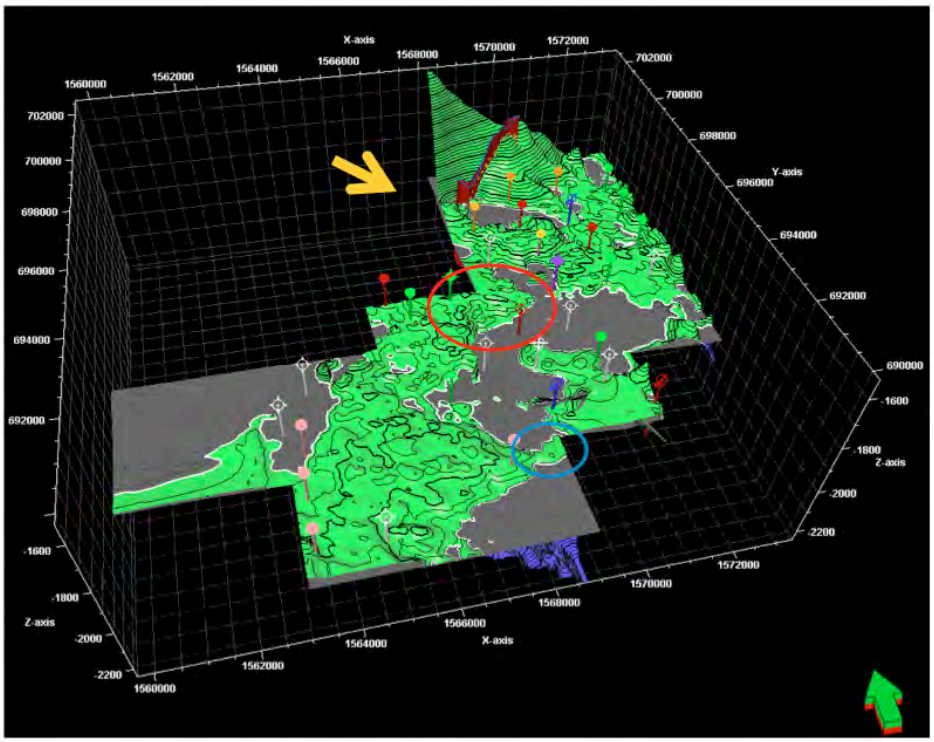

Figure 2. Depth-converted Mississippian reservoir top (green) and the oil-water contact (gray) to show the boundary of closure. Vertical to horizontal scale is 7.5:1 to magnify the difference in elevation. The depth conversion at the corner of the survey (yellow arrow) is not correct due to the lack of data to the northwest of the sealing fault (red surface).

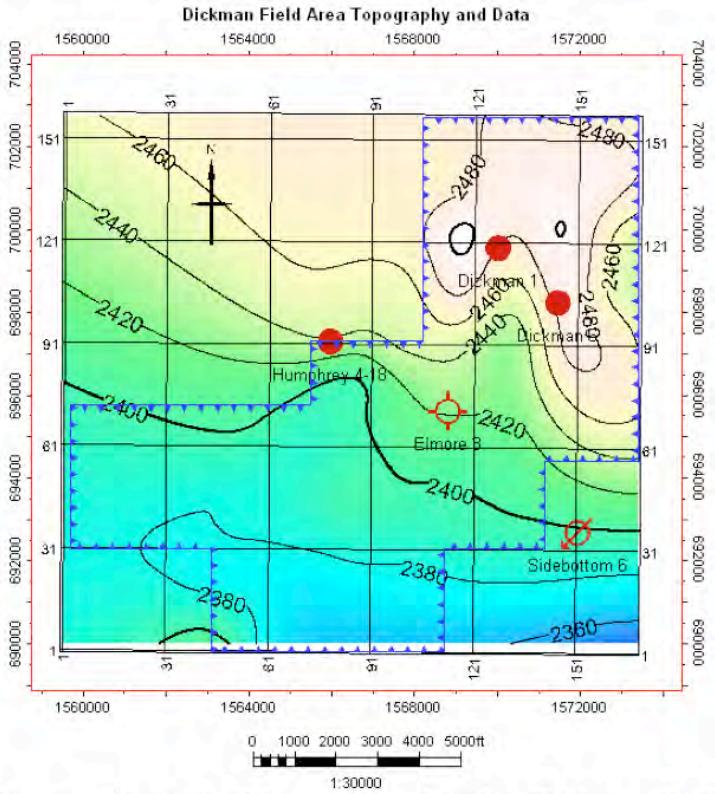

Figure 3. Local topography of the Dickman area and the five DT data wells. Three wells are producers (red dot), one dry hole (empty circle) and one injector (arrowed circle). Humphrey 4-18 and Sidebottom 6 wells have full penetration through the deep saline aquifer.

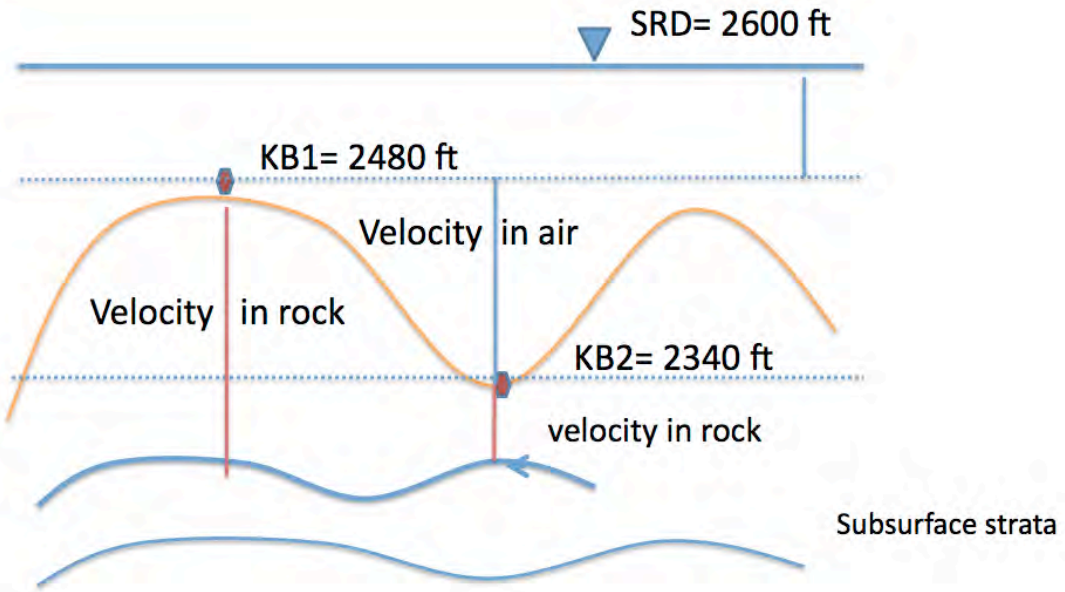

Figure 4. Topographic effect for well data as input to the stratigraphic-controlled velocity model. Thetopographic relief (brown line) is approximated by well KB. Red dots on the KB represent well locations, and blue lines at bottom represent subsurface strata.

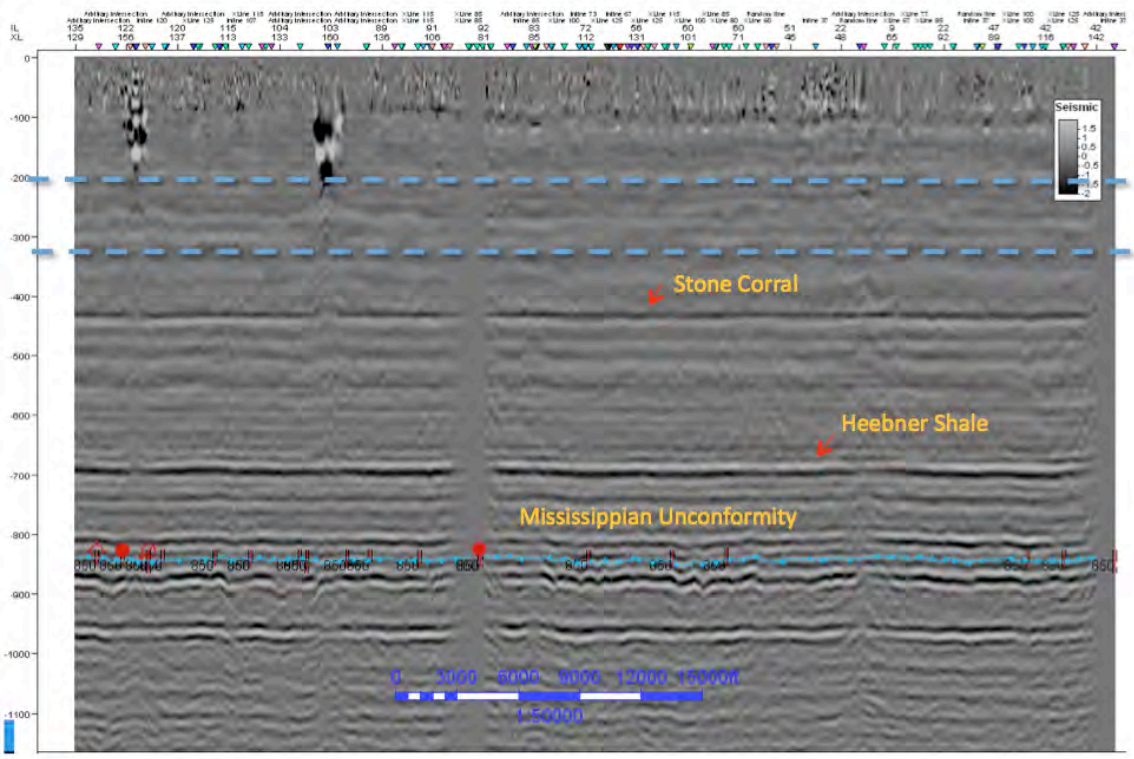

Figure 5. Cross-well section in seismic volume showing the relative locations of KB surfaces (between two dashed blue lines), the shallower stratigraphic target (yellow labels and arrows with no interpretation), and the deep target of the previous model (the Mississippian Unconformity as blue horizon). Red dots near Mississippian Unconformity are data wells.

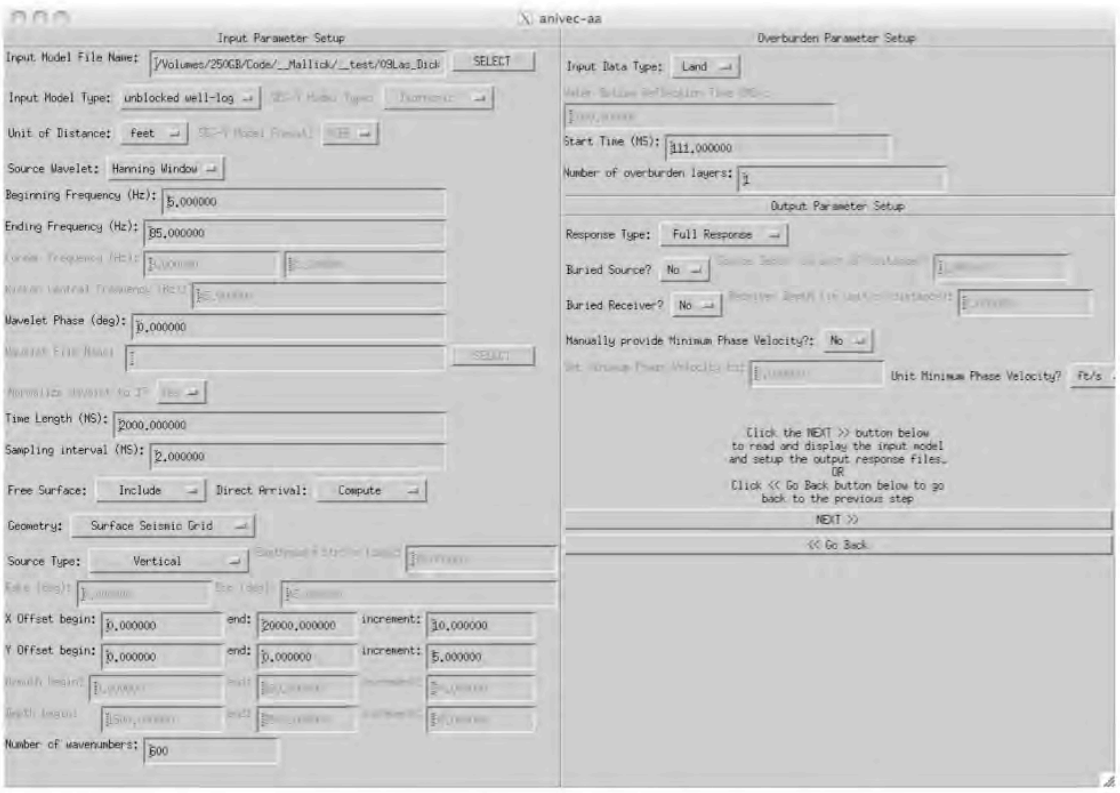

Figure 6. Input parameters for Anivec elastic forward modeling.

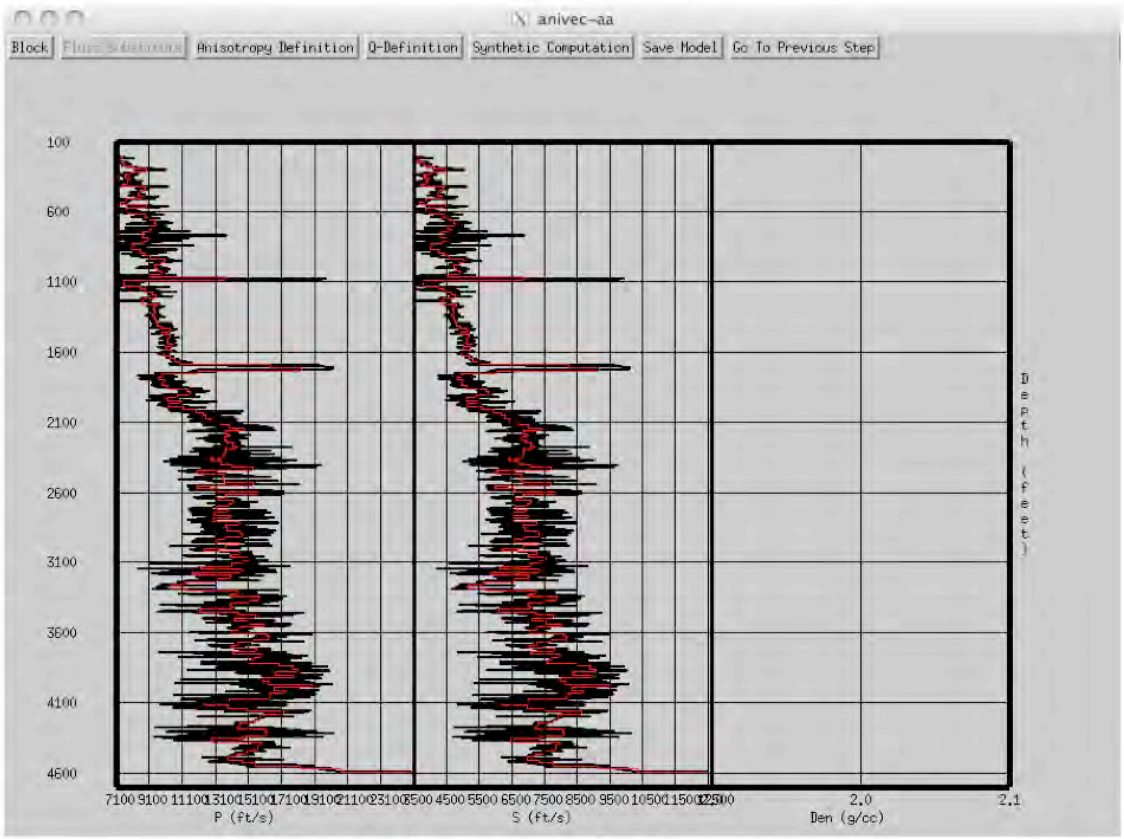

Figure 7. Vp and Vs for Anivec elastic forward modeling.

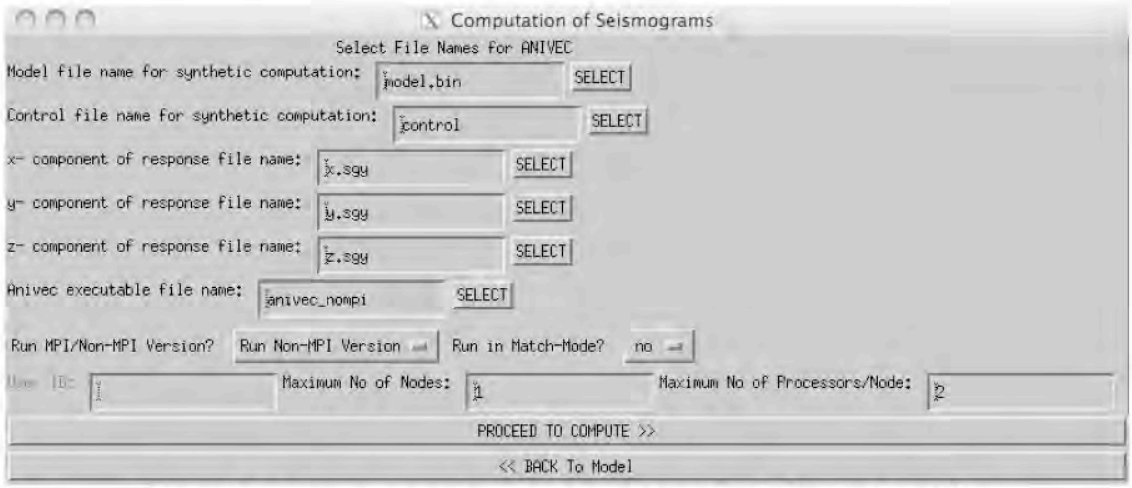

Figure 8. Output name assignment for Anivec elastic forward modeling.

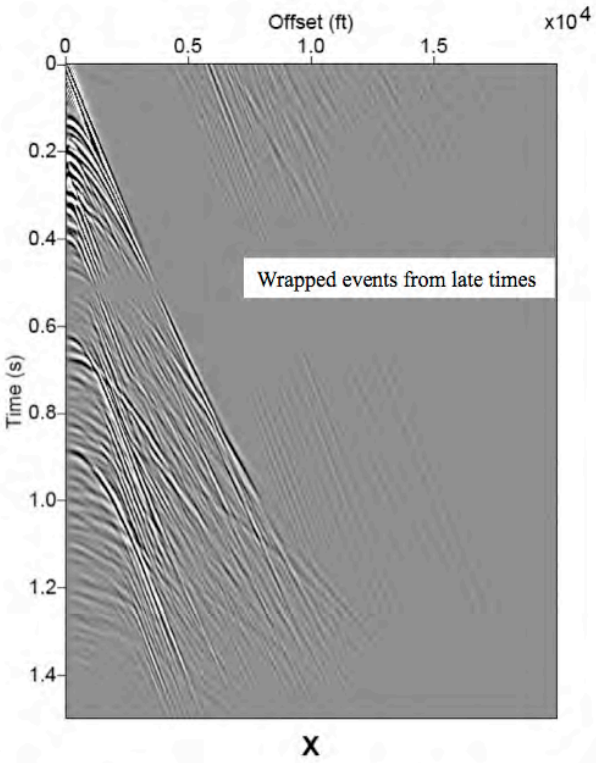

Figure 9. Radial component (x) of Anivec eastic forward modeling.

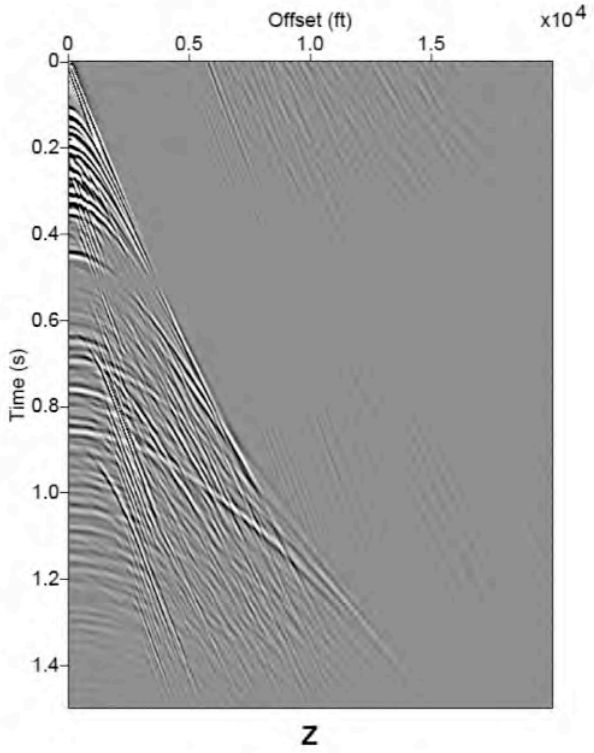

Figure 10. Vertical component (z) of Anivec elastic forward modeling.

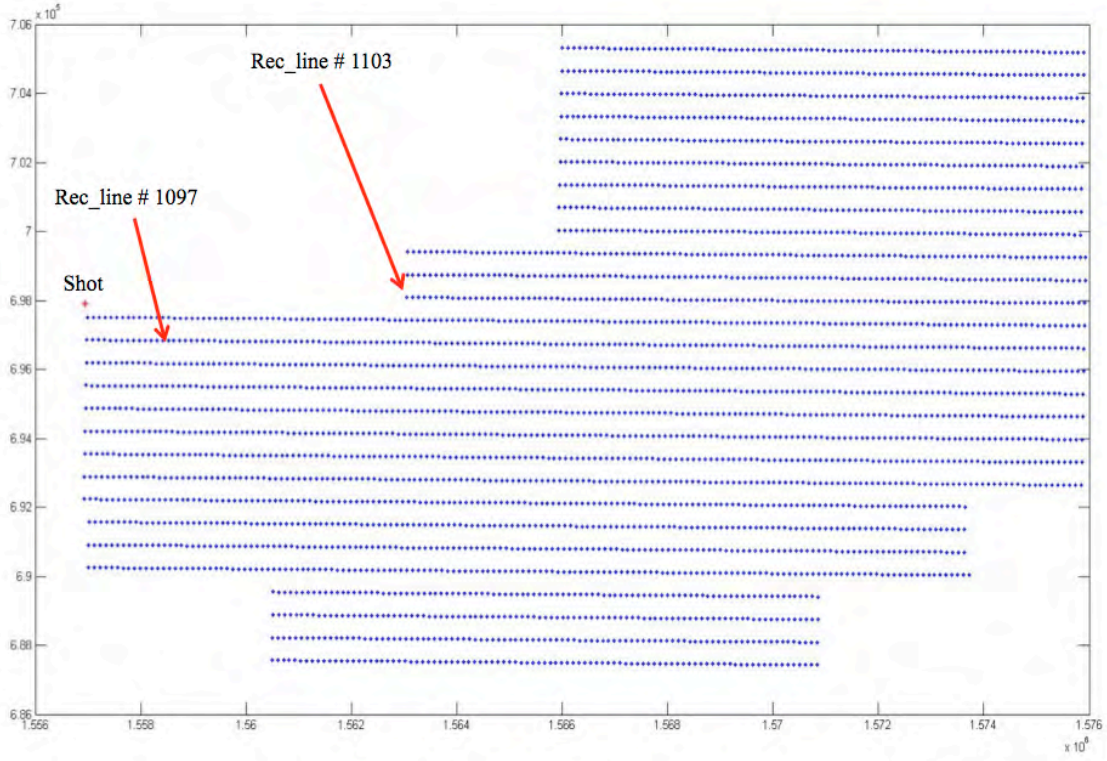

Figure 11. Geometry map shows receiver (blue dot) and one source (red dot).

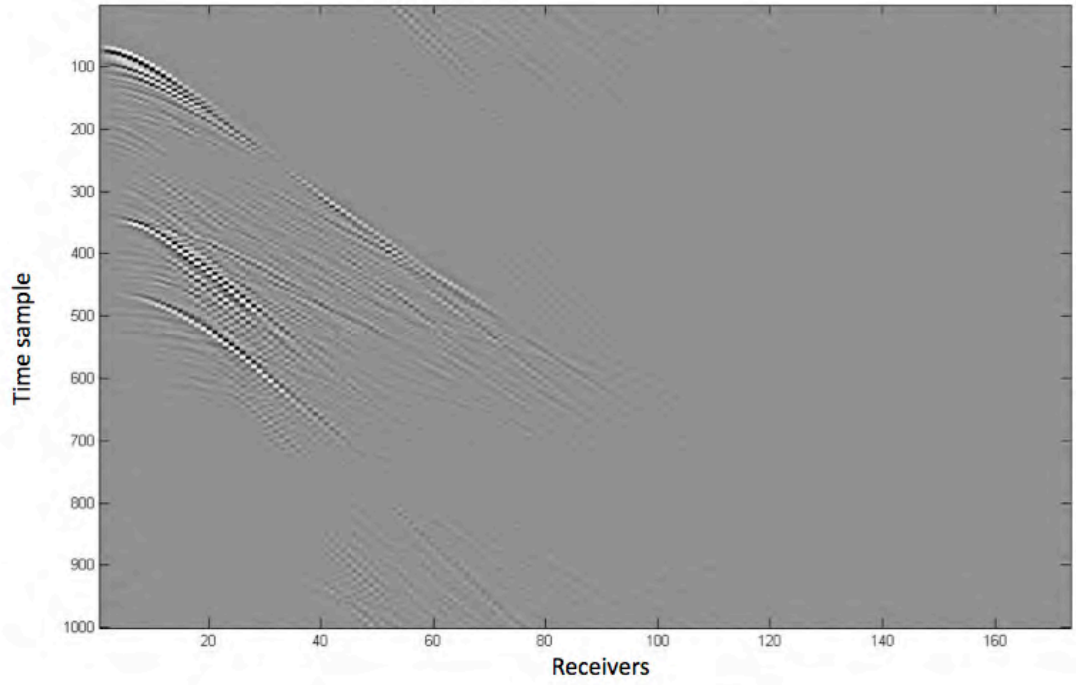

Figure 12 a) Seismic profile (radial component) of receiver line 1097, after horizontal rotation and trace population.

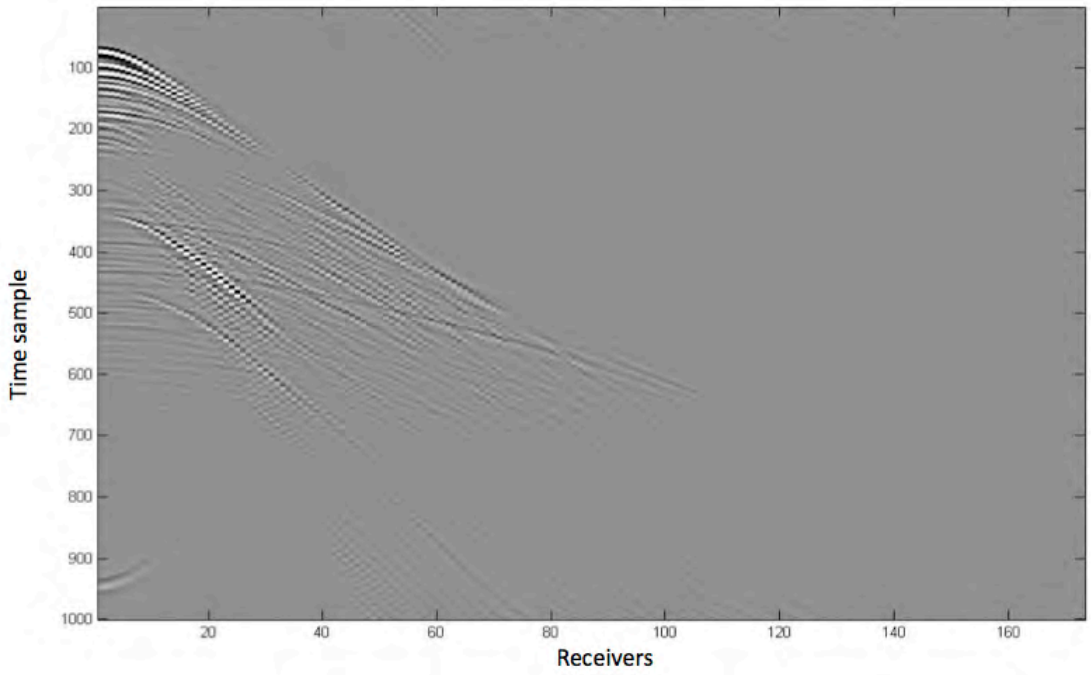

Figure 12 b) Seismic profile (vertical component) of the receiver line 1097, after trace population.

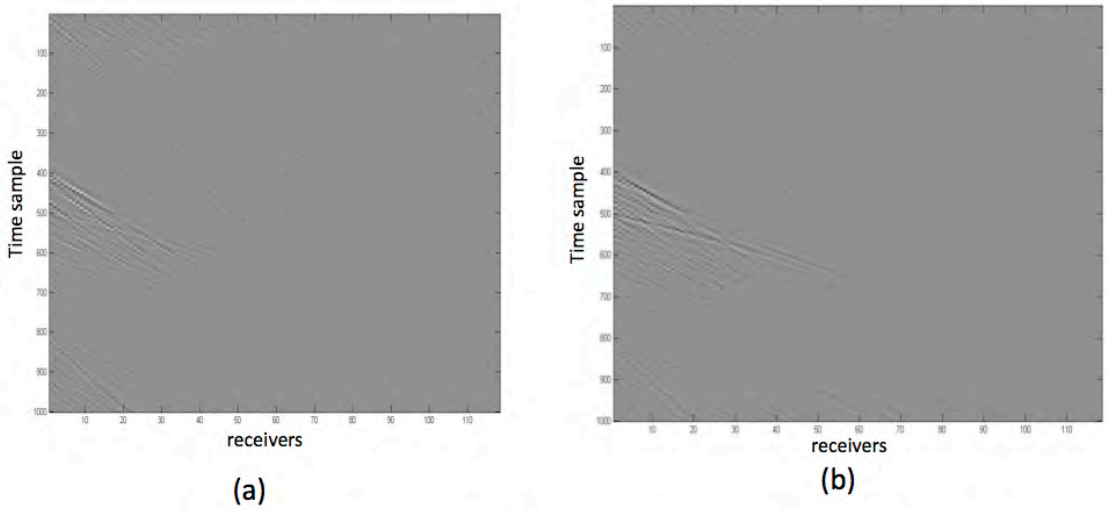

Figure 13. (a) Radial component and (b) vertical component of receiver line 1103.

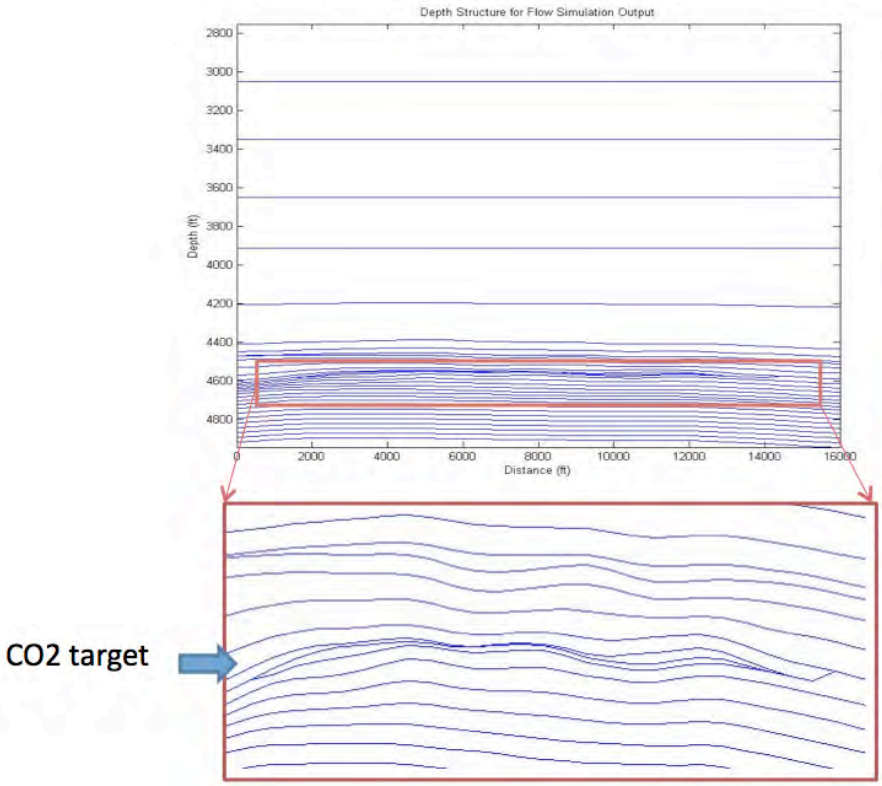

Figure 14. Geology structure for the simulation layers. Mississippian unconformity and porous carbonate can be indentified as CO2 sequestration target.

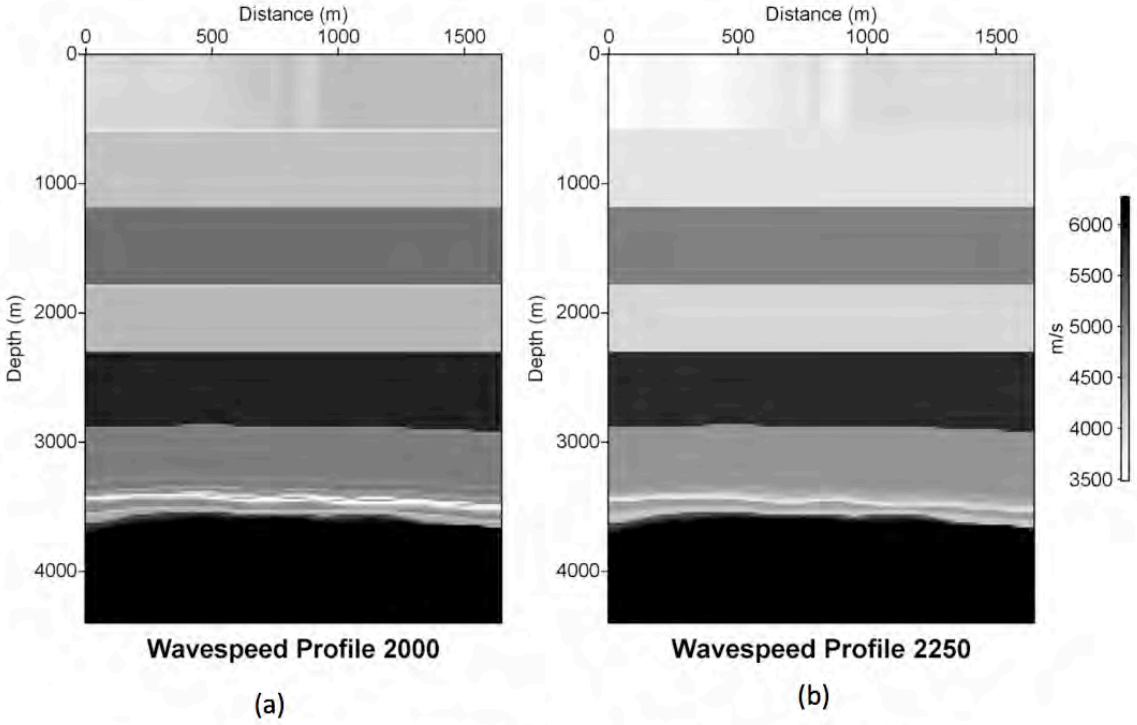

Figure 15. Calculated Velocity model for (a) Year 2000' and (b) 2250'.

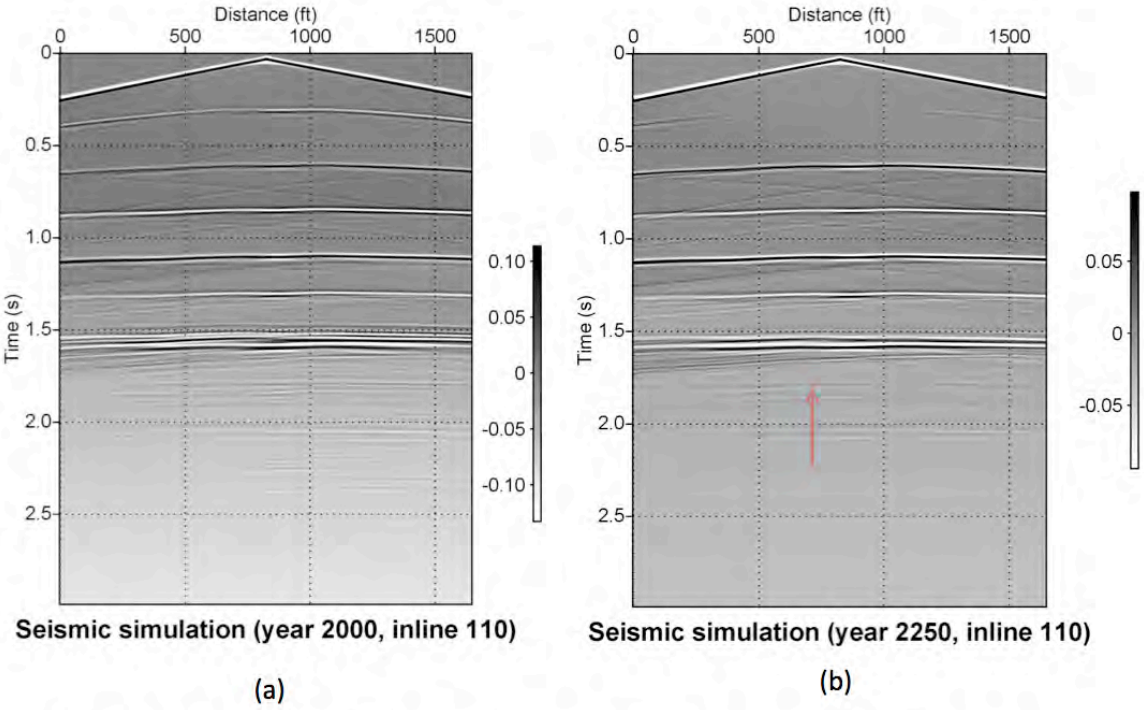

Figure 16. Acoustic forward modeling result with point source (a) first year of injection (b) last year of monitoring. Red arrow shoindicates area of difference.

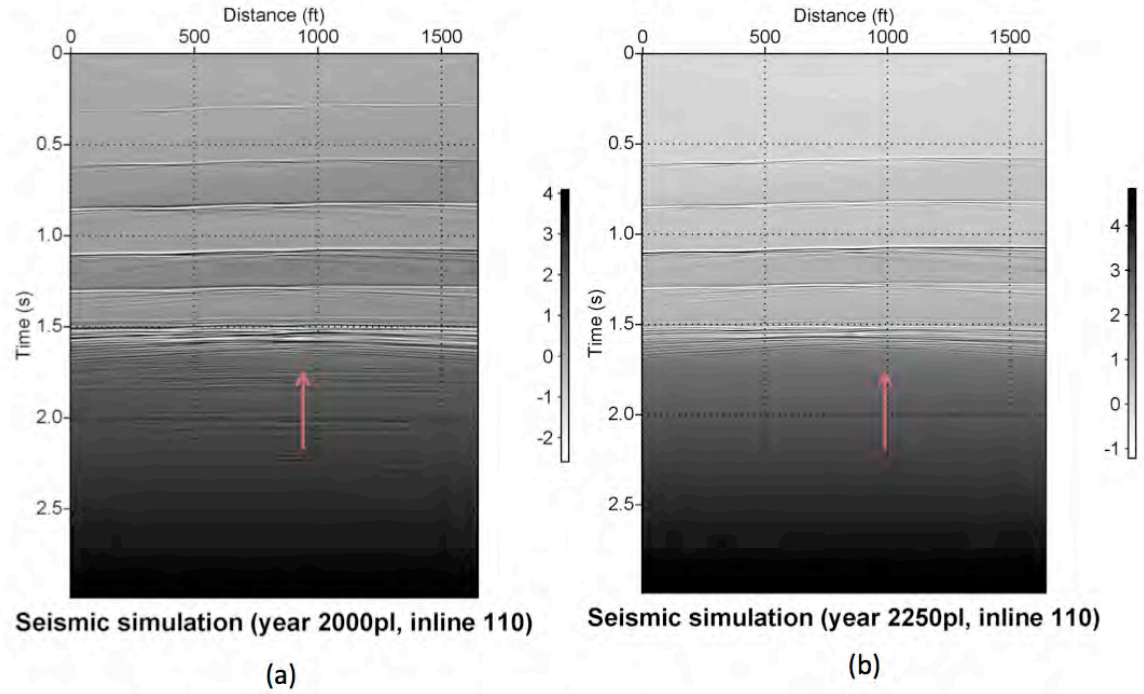

Figure 17. Acoustic forward modeling result with plane wave source. (a) first year of injection. (b) last year of monitoring. Red arrow indicates area of difference.

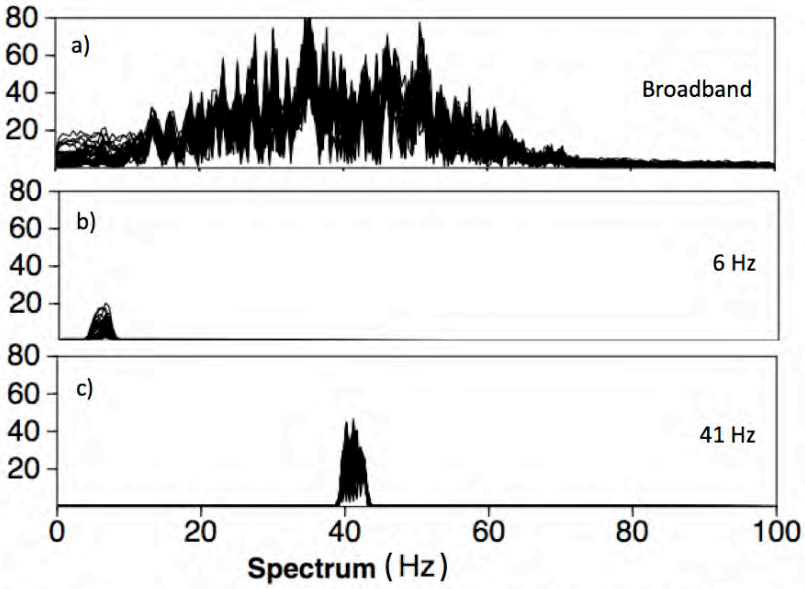

Figure 18: Survey spectra created in SU for (a) broadband data, (b) 6 Hz data created with 2 Hz top filter where fracture indicators are present and (c) 41 Hz data created with 2 Hz top filter where channel indicators are present.

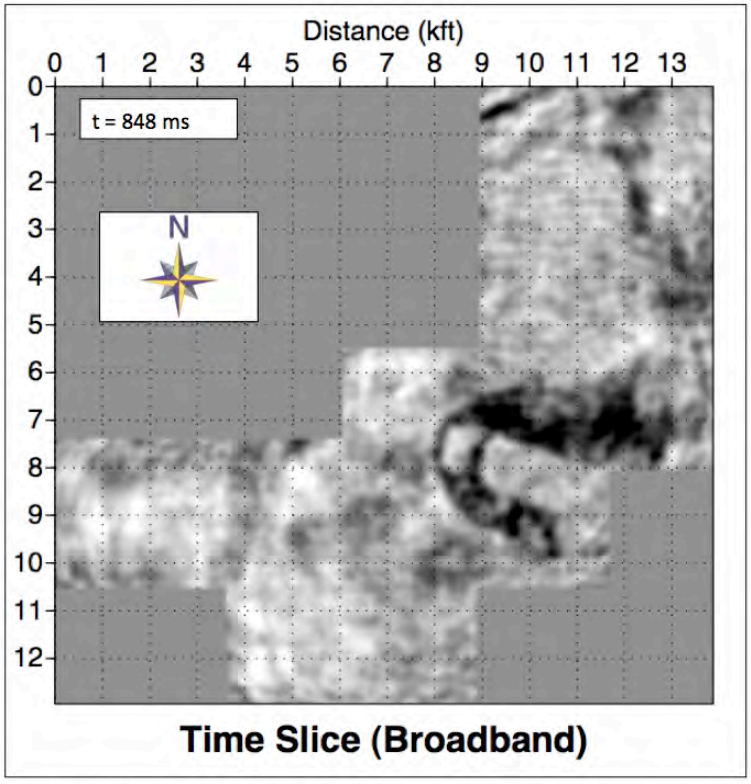

Figure 19: Timeslice at 848 ms showing the broadband data with no fracture or tributary channel indicators.

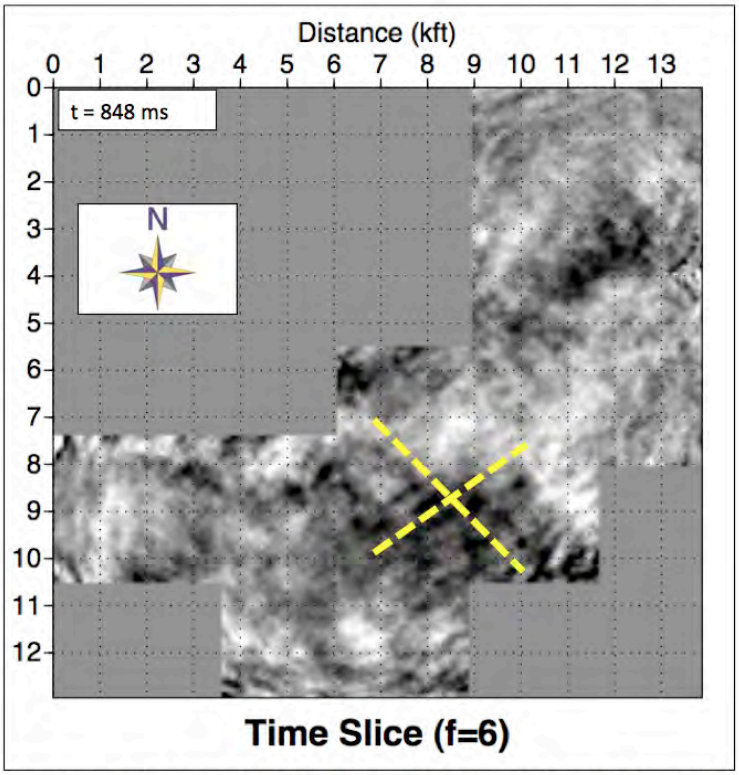

Figure 20: Timeslice at 848 ms of the 6 Hz data with NE to SW and NW to SW lineations indicated by yellow dashed lines, and curved lineations near the edges, believed to be edge effects.

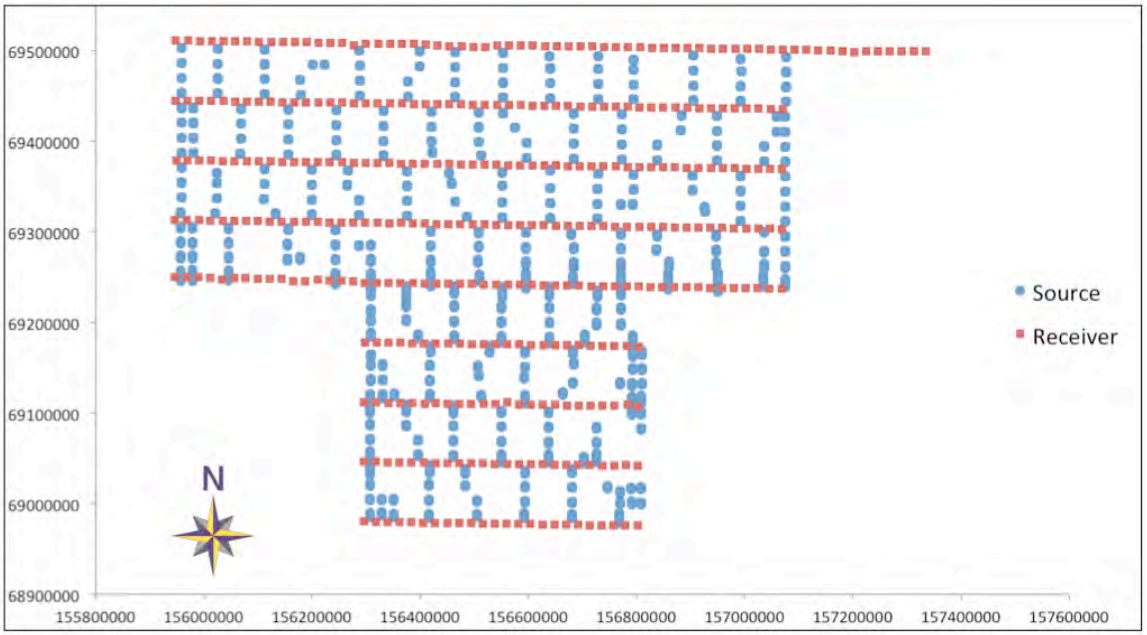

Figure 21: Survey Design for the Dickman Field. Shooting geometry does not correlate with the linear features in Figure 20, meaning they cannot be attributed to acquisition footprint.

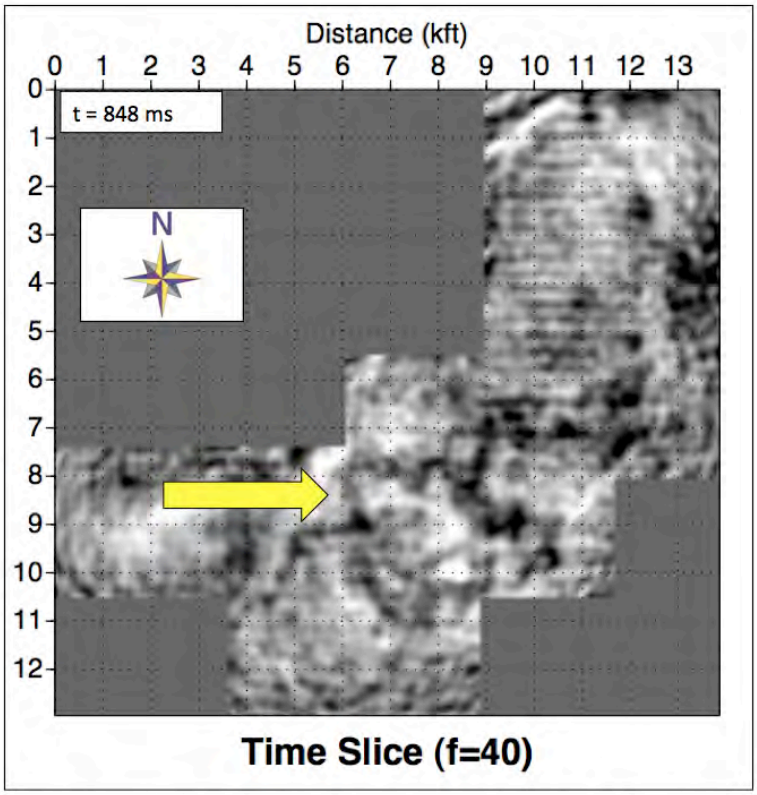

Figure 22: Timeslice at 848 ms of the 40 Hz data showing a possible channel feature, indicated by a yellow arrow, not seen in the broadband data to the west of the main channel.

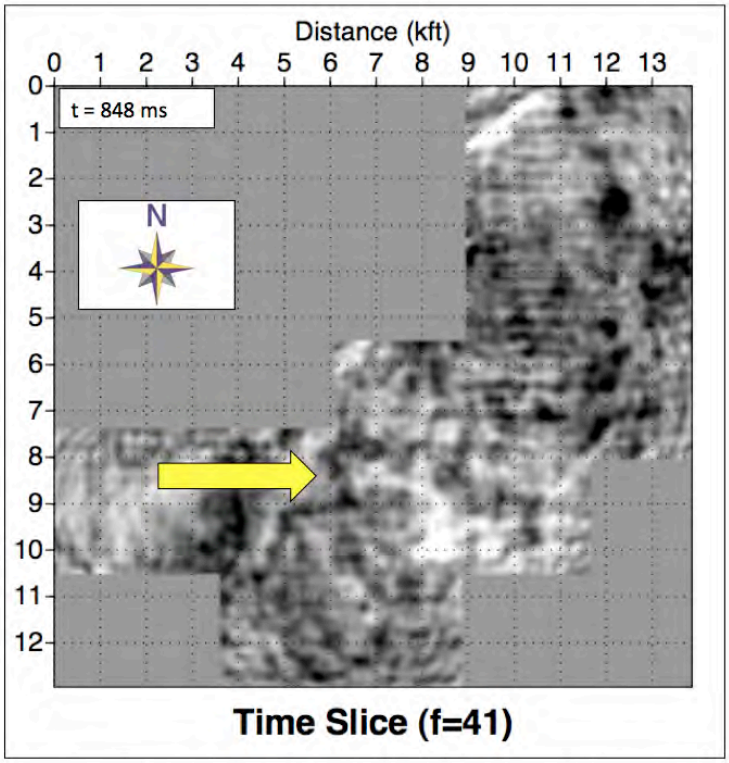

Figure 23: Timeslice at 848 ms of the 41 Hz data showing a possible channel feature, indicated by a yellow arrow, not seen in the broadband data to the west of the main channel.

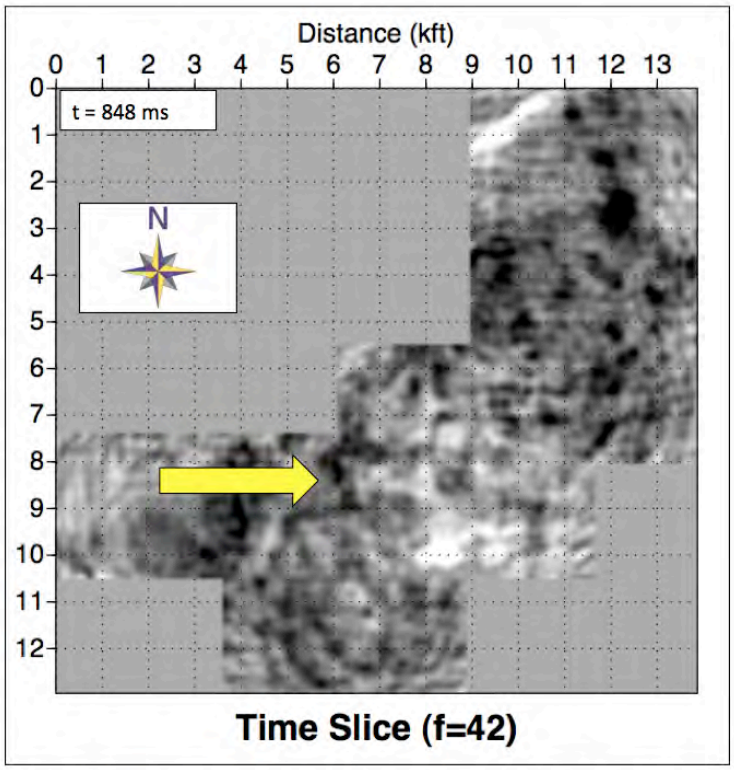

Figure 24: Timeslice at 848 ms of the 42 Hz data showing a possible channel feature, indicated by a yellow arrow, not seen in the broadband data to the west of the main channel.

Figure 25: The yellow circle shows a modern analog of a tributary type channel feeding into a main channel in coastal Georgia.

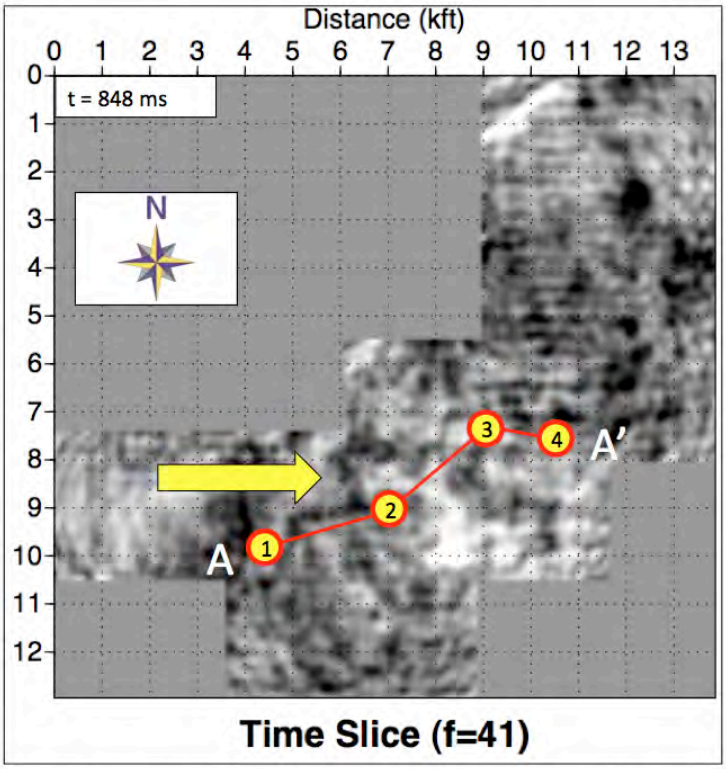

Figure 26: Line of cross section from A to A' showing the expected channel location indicated by the yellow arrow and numbered well locations located in or near channel features.

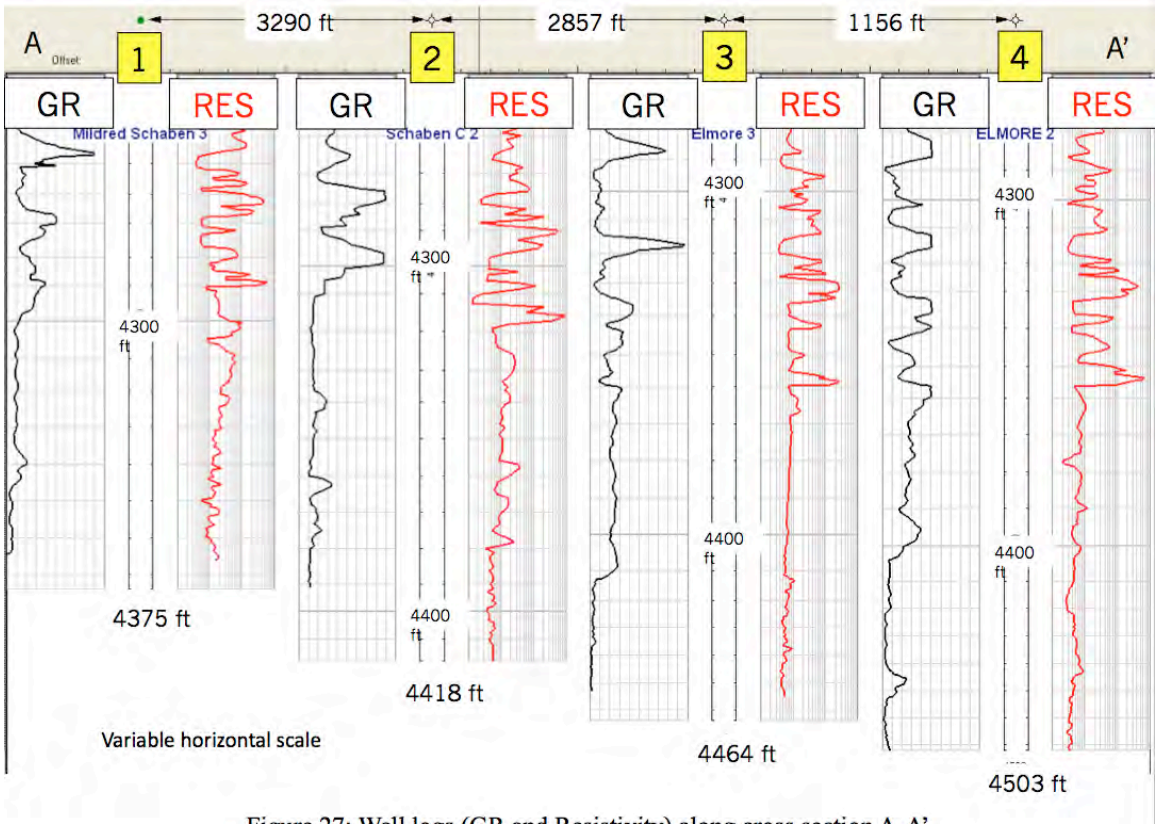

Figure 27: Well logs (GR and Resistivity) along cross section A-A'.

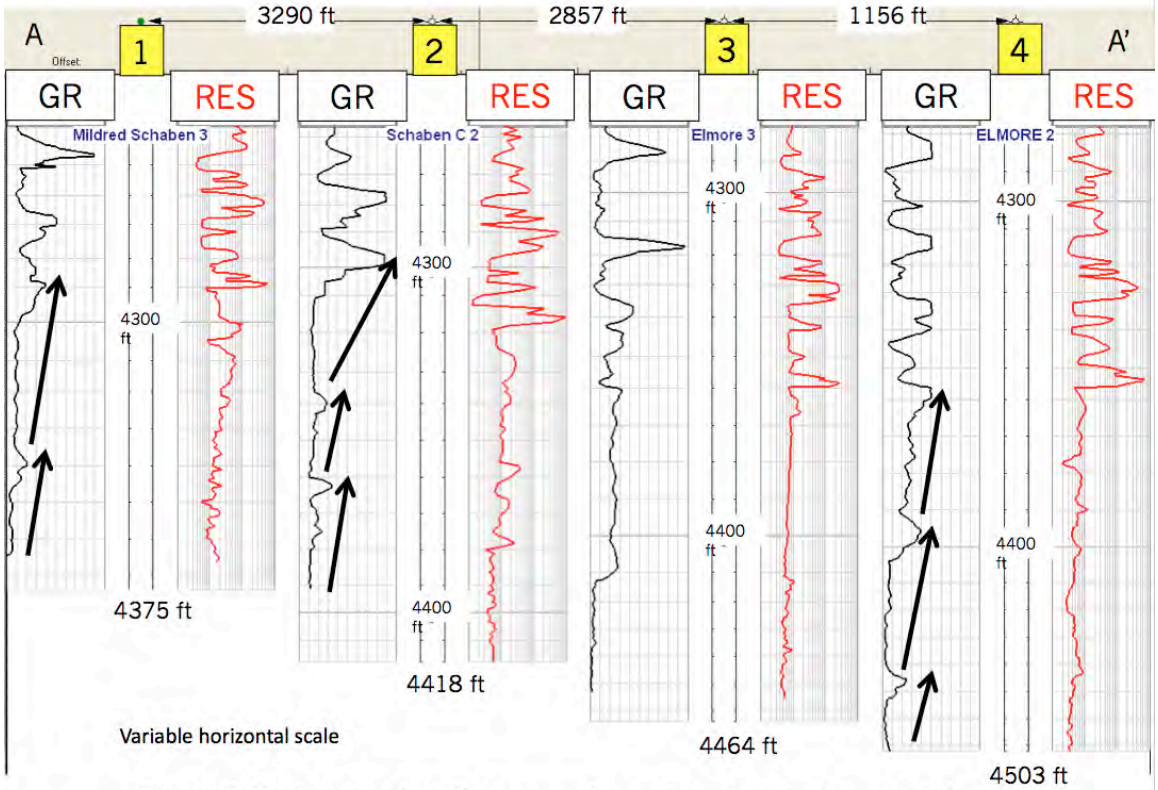

Figure 28: Black arrows show fining upwards sequences from sandstone to shale indicating a channel-like depositional environment.

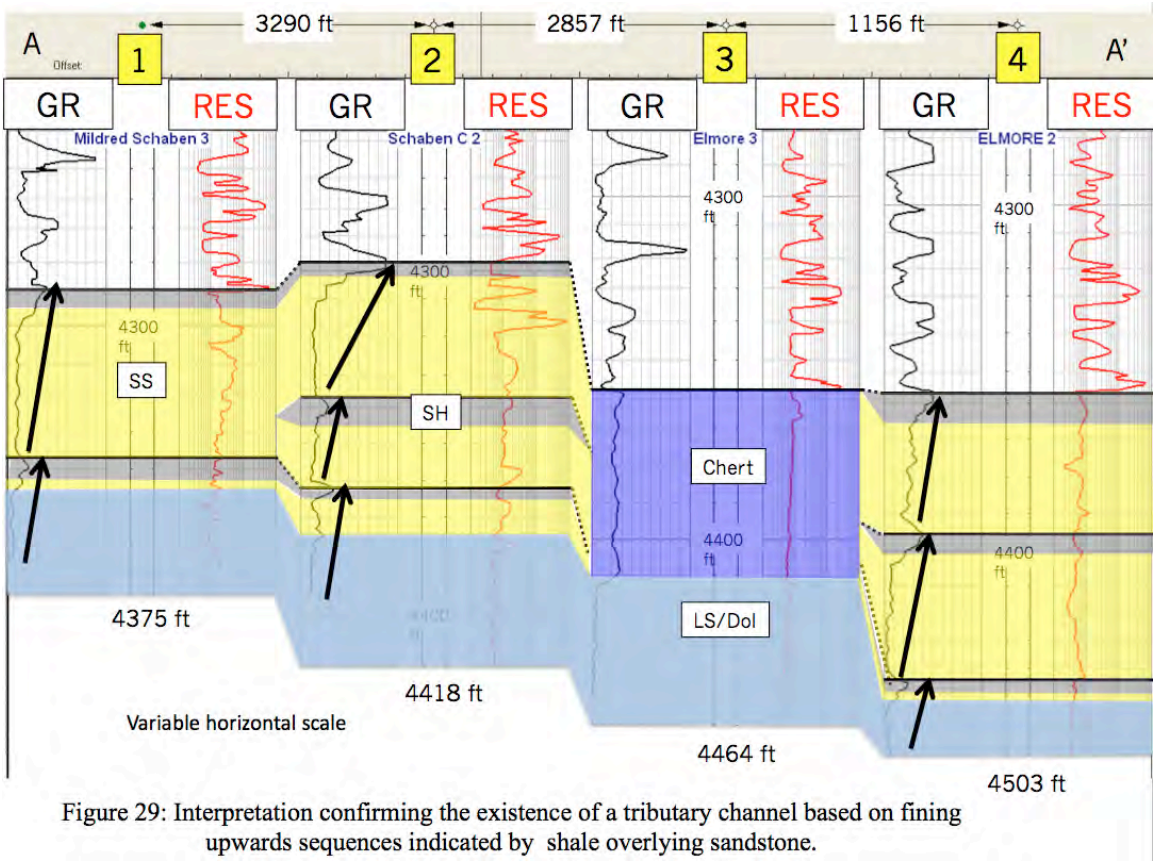

Figure 29: Interpretation confirming the existence of a tributary channel based on fining upwards sequences indicated by shale overlying sandstone.

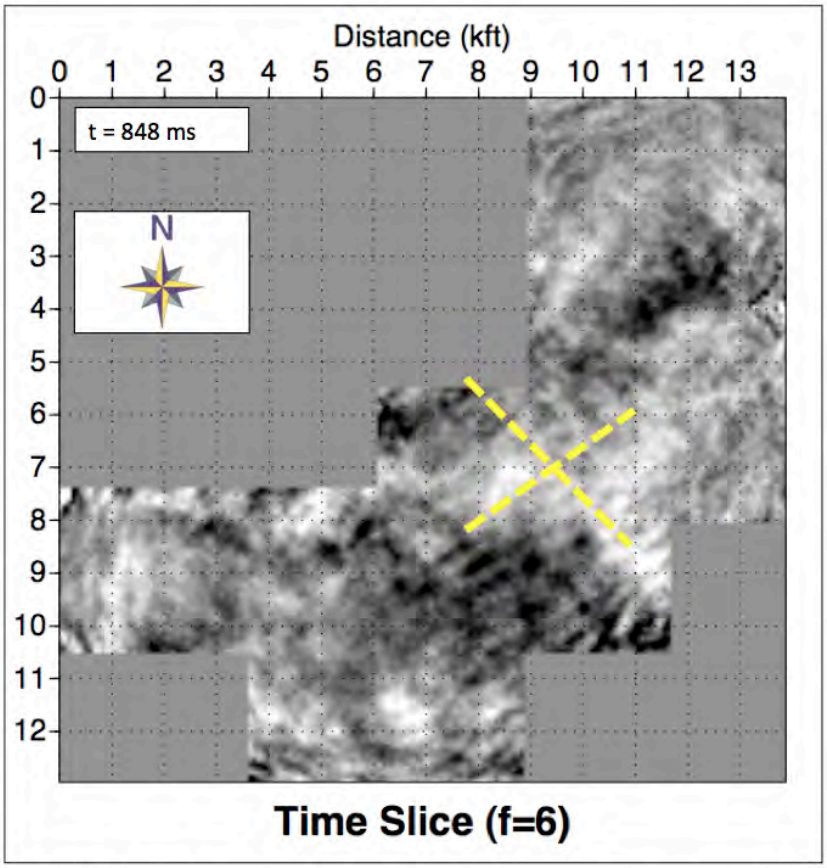

Figure 30. 6 Hz slice at 848 ms showing NE-NW trending features that are potentially related to fracture networks. Yellow dashed lines represent the respective orientations.

Well log	Response to fracture
Gamma Ray	High gamma ray spike due to clay filled fracture
Sonic	Long travel time spike due to cycle skipping
Density	Reduction in density due to mud invasion
Density Correction	Large density correction in stiff rock due to compensation from mud invasion
Caliper	Borehole elongation due to fractured interval
Shallow/Deep Induction	Resistivity curves will converge or shallow will crossover reading a smaller resistivity value due to mud invasion
Micro Resistivity	Low resistivity spike due to filtrate invasion

Figure 31. showing conventional well logs used for fracture characterization and associated response.

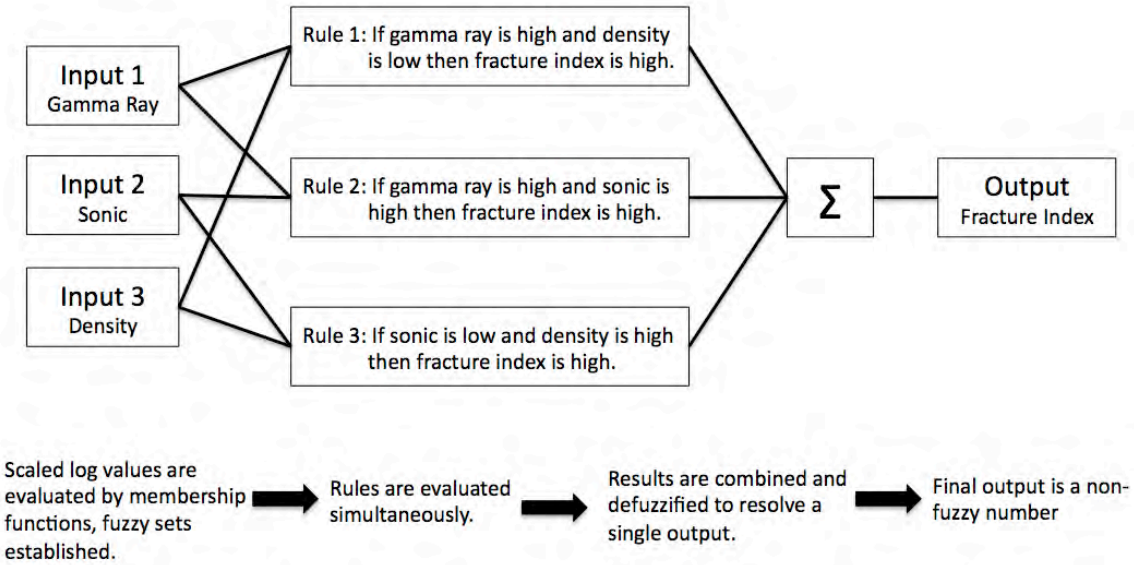

Figure 32. Schematic describing the structure of a fuzzy inference system. The process consists of the following parts: fuzzification of the input, application of the linguistic operators, the composition of the rules, and the defuzzification process which accounts for interference of the output fuzzy set.

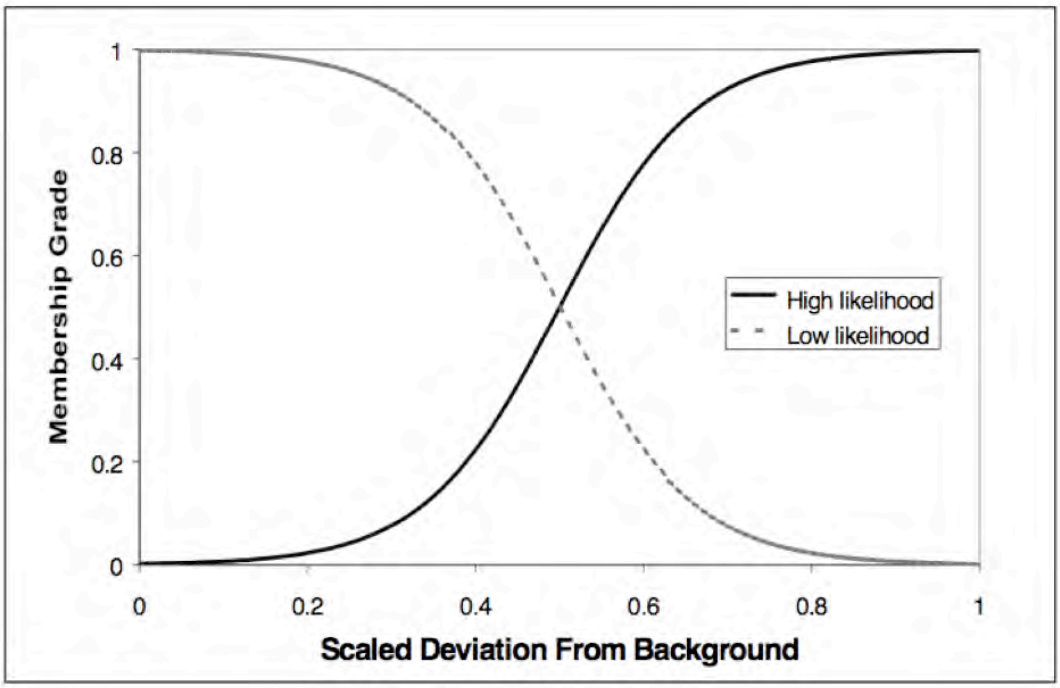

Figure 33. Sigmoidal membership functions designating two fuzzy sets, high likelihood and low likelihood of fractures (after Martinez et al., 2001). Scaled log values will be assigned a membership grade then an output grade based on linguistic operators.

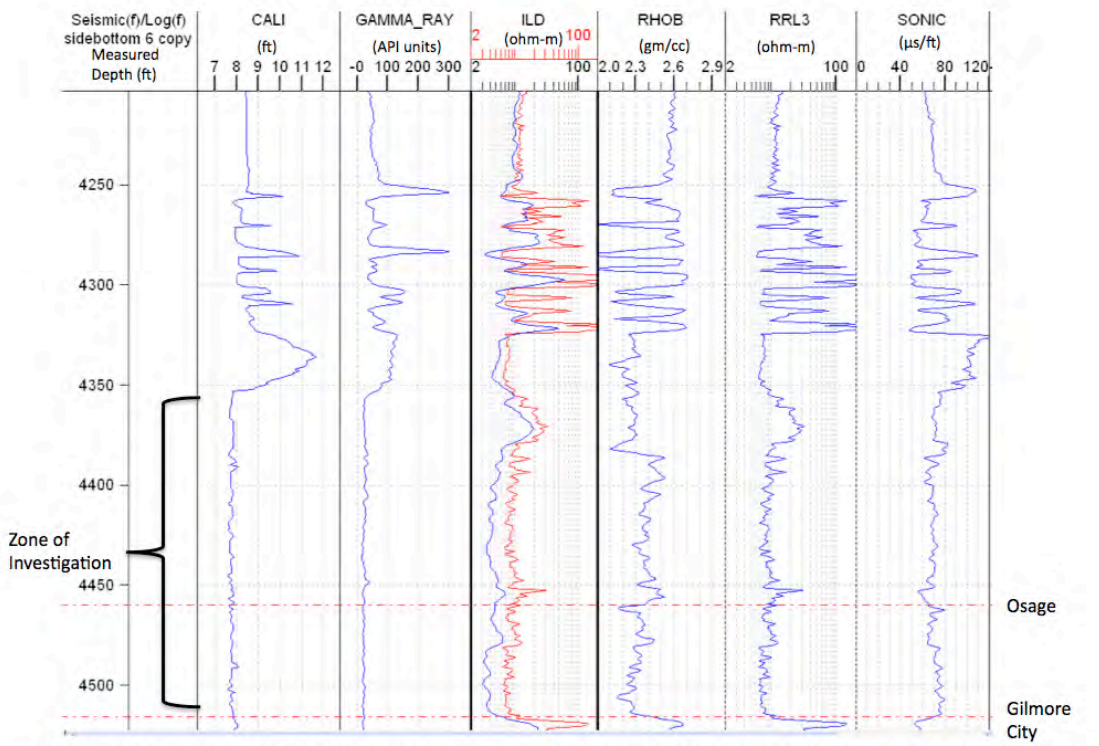

Figure 34. Well logs used from Sidebottom 6 for an experimental FIS. From left to right the logs used are: caliper, gamma ray, deep induction with shallow resistivity as a reference in red, density, shallow resistivity, and sonic. The zone of investigation is the Mississippian carbonate just below the unconformity spanning from 4360-4510 ft measured depth.

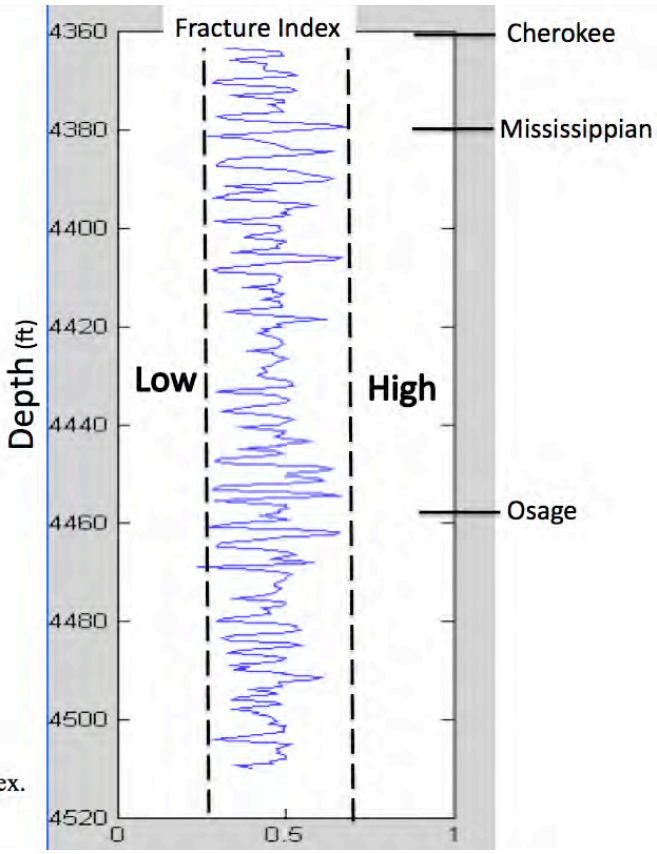

Figure 35. Fracture index.

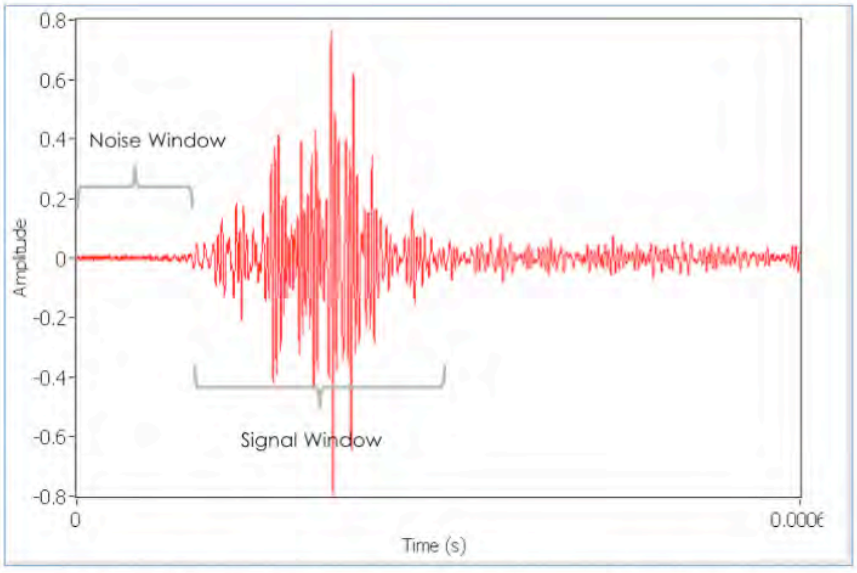

Figure 36: Waveform with noise window and signal window

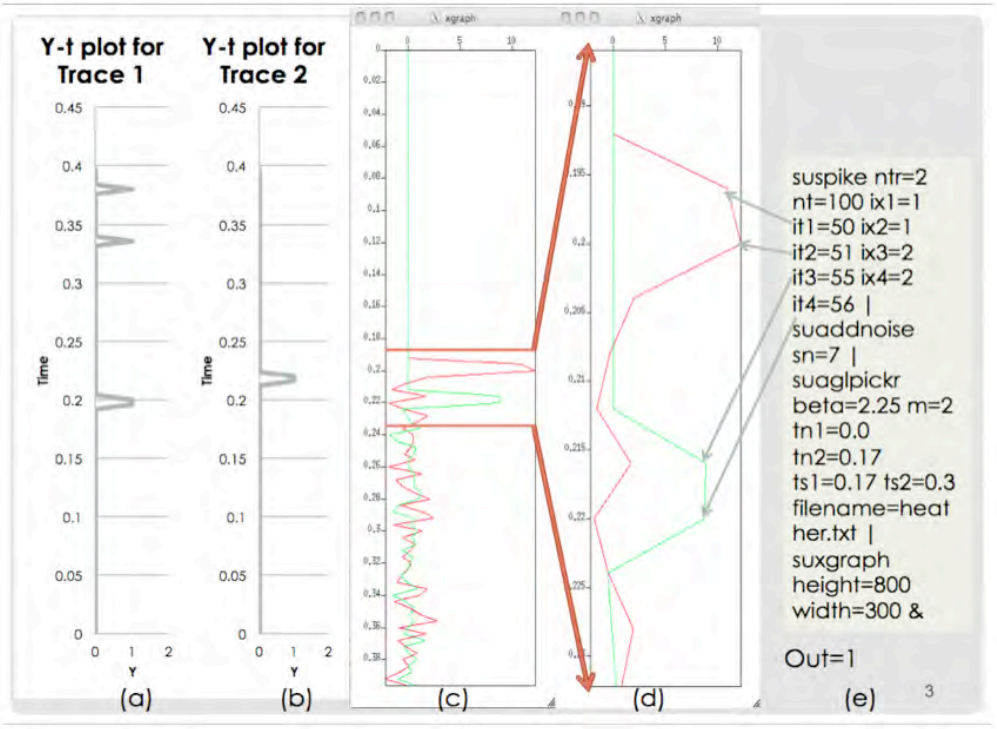

Figure 37. (a) Y-t plot for trace 1 (b) Y-t plot for trace 2 (c) output traces (d) Zoom in for output traces (e) source code

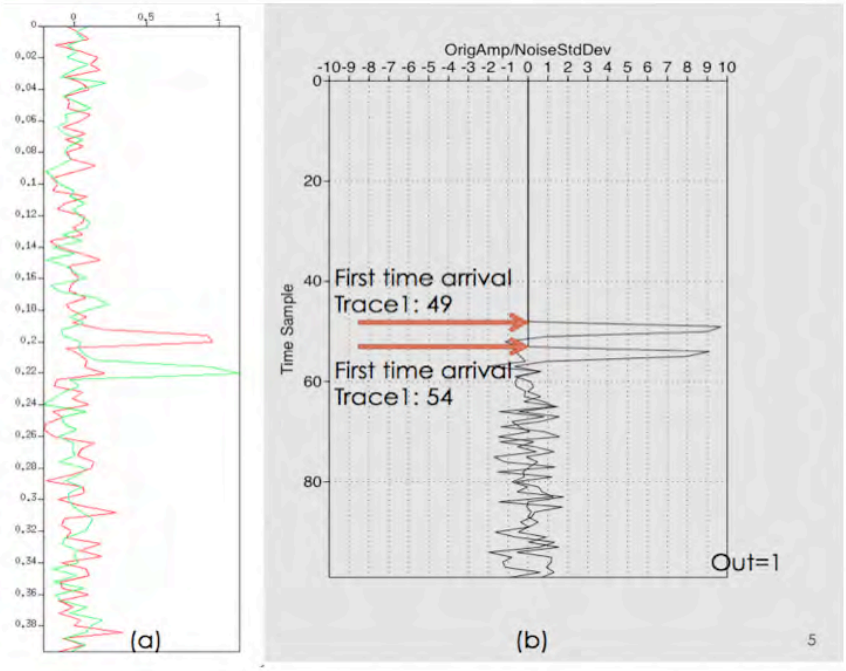

Figure 38. (a) input trace (b) output trace: amplitude / time sample number

```
Noise window(s) : 0.000000 0.170000
Signal window(s) : 0.170000 0.300000
Signal window length : 34
beta : 2.250000
m : 2
i : 49
dt : 0.004000
Probability of error : 0.024449
First time arrival sample number : 49
First time arrival time(s) : 0.192000
Probability of false positive anywhere : 0.020125
```

Figure 39. Output text file data for trace 1.

```
Noise window(s) : 0.000000 0.170000
Signal window(s) : 0.170000 0.300000
Signal window length : 34
beta : 2.250000
m : 2
i : 54
dt : 0.004000
Probability of error : 0.024449
First time arrival sample number : 54
First time arrival time(s) : 0.212000
Probability of false positive anywhere : 0.020125
```

Figure 40. Output text file data for trace 2.

```
trace number : 2
trace_number : 0 pick_time(s) : 0.192000
trace_number : 1 pick_time(s) : 0.212000
mean first pick time(s) : 0.202000
val : 0.000200
standard deviation for first pick time(s) : 0.014142
```

Figure 41. Output results for the traces

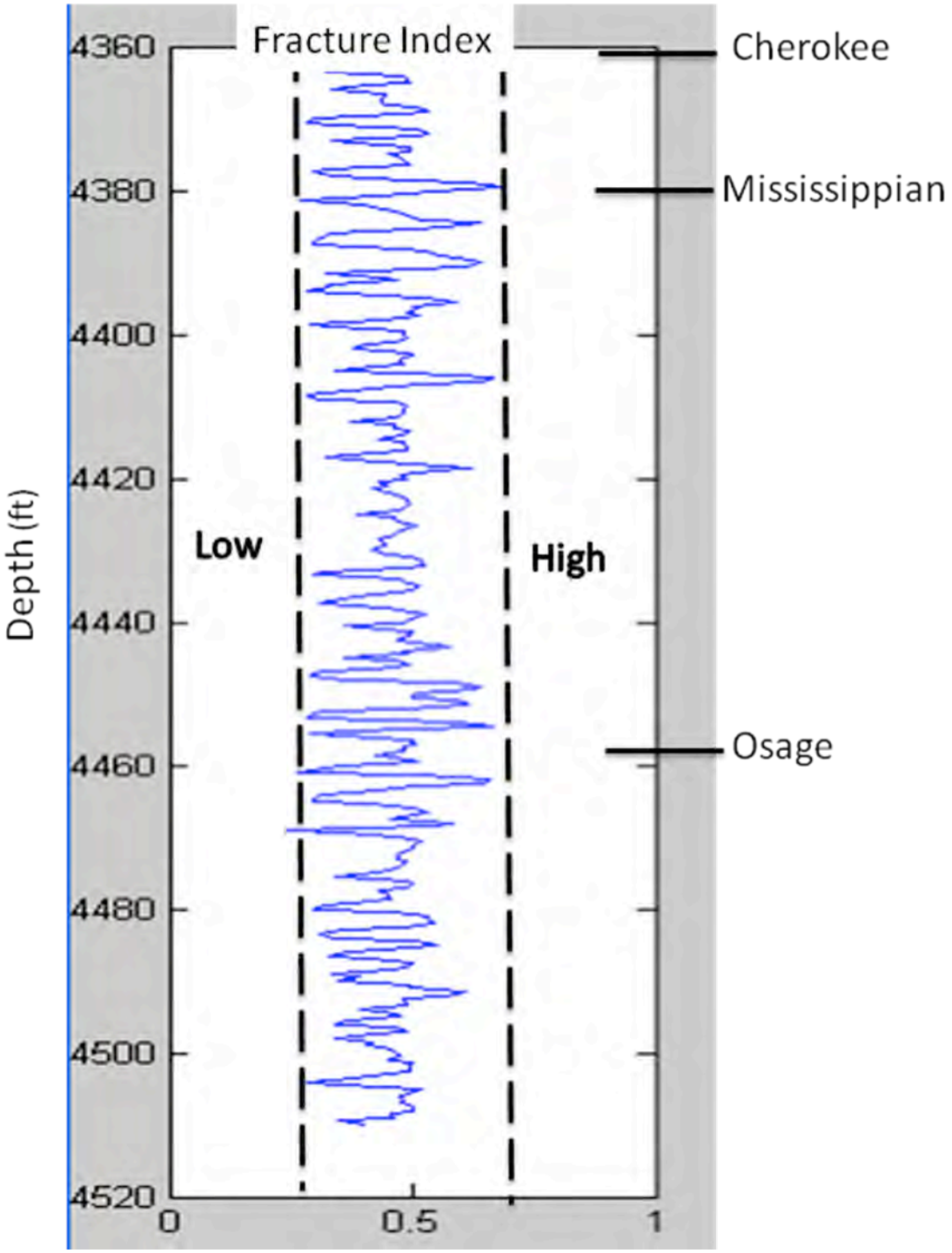
Fracture Index
Cherokee
Mississippian
Osage
Depth (ft)
4360
4380
4400
4420
4440
4460
4480
4500
4520
Low
High
0
0.5
1